Winter and spring evolution of northern seasonal deposits on Mars from OMEGA on Mars Express

T. Appéré,[1] B. Schmitt,[1] Y. Langevin,[2] S. Douté,[1] A. Pommerol,[1,3] F. Forget,[4] A. Spiga,[4] B. Gondet,[2] and J.-P. Bibring[2]

[1] The OMEGA visible/near-infrared imaging spectrometer on Mars Express has observed the retreat of the northern seasonal deposits during Martian year 27–28 from the period of maximum extension, close to the northern winter solstice, to the end of the retreat at L_s 95°. We present the temporal and spatial distributions of both CO_2 and H_2O ices and propose a scenario that describes the winter and spring evolution of the northern seasonal deposits. During winter, the CO_2-rich condensates are initially transparent and could be in slab form. A water ice annulus surrounds the sublimating CO_2 ice, extending over 6° of latitude at L_s 320°, decreasing to 2° at L_s 350°, and gradually increasing to 4.5° at L_s 50°. This annulus first consists of thin frost as observed by the Viking Lander 2 and is then overlaid by H_2O grains trapped in the CO_2-rich ice layer and released during CO_2 sublimation. By L_s 50°, H_2O ice spectrally dominates most of the deposits. In order to hide the still several tens of centimeters thick CO_2 ice layer in central areas of the cap we propose the buildup of an optically thick top layer of H_2O ice from ice grains previously embedded in the CO_2 ice and by cold trapping of water vapor from the sublimating water ice annulus. The CO_2 ice signature locally reappears between L_s 50° and 70°. What emerges from our observations is a very active surface-atmosphere water cycle. These data provide additional constraints to the general circulation models simulating the Martian climate.

1. Introduction

[2] The formation and sublimation of seasonal deposits on the surface of Mars are major elements controlling its atmospheric circulation and its climate. Asymmetric cyclic seasonal variations of the surface pressure of up to ~30% have been measured by Viking landers [*Tillman et al.*, 1993]. Global circulation models have shown that these changes in total atmospheric mass are induced by a complex competition between sublimation of CO_2 frost from one hemisphere, interhemispheric transport and recondensation at the surface of the opposite polar regions [*Hourdin et al.*, 1993; *Forget et al.*, 1998].

[3] Ground-based observations of the seasonal deposits have been limited to retreat phases as caps are tilted away

from the Sun and Earth during the formation phases. Terrestrial observations of the receding northern seasonal deposits have been obtained during aphelic oppositions when Mars is relatively small in diameter, and even then the poles were near the limb, thus preventing a reliable analysis of the range of phenomena encountered and their variability. *Antoniadi* [1930] and *Fischbacher et al.* [1969] summarized many of these early terrestrial observations and *Cantor et al.* [1998] reported on the Hubble Space Telescope (HST) observations of several north polar retreats.

[4] Spacecraft orbiting Mars have documented the evolution of the northern seasonal deposits with much higher spatial resolution. Mariner 9 acquired three synoptic views of the northern seasonal deposits in mid-late spring of Martian year 10 [*Soderblom et al.*, 1973] and Viking orbiters also monitored the spring retreat of the deposits in Martian years 12 and 13 [*James*, 1979, 1982] (Martian years (MY) defined by *Clancy et al.* [2000] began with MY 1 starting at the 1955 vernal equinox, $L_s = 0°$, where L_s is the aerocentric longitude of the Sun). However, the orbits of Viking spacecraft were not favorable for synoptic observations of the seasonal deposits since the resolution near Viking periapsis was too high to allow monitoring more than a small longitude. Mars Orbiter Camera (MOC) and Thermal Emission Spectrometer

[1]Institut de Planétologie et d'Astrophysique de Grenoble, Université J. Fourier, CNRS/INSU, Grenoble, France.
[2]Institut d'Astrophysique Spatiale, Université Paris-Sud XI, CNRS/INSU, Orsay, France.
[3]Now at Physikalisches Institut, Universität Bern, Bern, Switzerland.
[4]Laboratoire de Météorologie Dynamique, IPSL, CNRS/INSU, Université Pierre et Marie Curie, Paris, France.
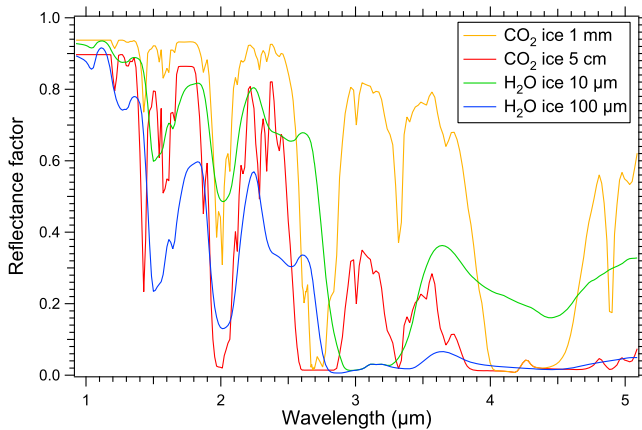
Figure 1. Spectra of CO_2 ice with grain sizes of 1 mm (orange) and 5 cm (red) and H_2O ice with grain sizes of 10 μm (green) and 100 μm (blue) modeled using a radiative transfer code developed by *Douté and Schmitt* [1998] and optical constants of H_2O ice [*Grundy and Schmitt*, 1998; *Schmitt et al.*, 1998] and CO_2 ice [*Quirico and Schmitt*, 1997; *Schmitt et al.*, 1998].

(TES) instruments aboard the Mars Global Surveyor (MGS) spacecraft monitored four complete spring retreats of the northern seasonal deposits between 1999 and 2006 (MYs 25 to 28) [*James and Cantor*, 2001; *Benson and James*, 2005; *Kieffer and Titus*, 2001]. More recently, the Mars Reconnaissance Orbiter Mars Color Imager (MARCI) instrument aboard Mars Reconnaissance Orbiter (MRO) recorded the MY 29 spring retreat [*Cantor et al.*, 2010].

[5] Near-infrared spectrometry [*Herr and Pimentel*, 1969; *Larson and Fink*, 1972; *Calvin and Martin*, 1994] and observations in the thermal infrared [*Neugebauer et al.*, 1971; *Kieffer*, 1979; *Kieffer et al.*, 2000] demonstrated that CO_2 ice is the major component of the seasonal deposits. It was previously proposed that there might be an annulus of water ice just south of the receding CO_2 ice condensates [*Houben et al.*, 1997]. The similarity in reflectance between CO_2 and H_2O ices makes the distinction difficult in the visible range. Thermal infrared observations may partially resolve the composition of the ices since regions covered by CO_2 frost have a temperature <150 K due to the thermodynamic equilibrium with the atmosphere. Brightness temperatures in the 160 to 180 K range provide evidence for H_2O frost coverage, but such intermediate temperatures can also result from spatial mixing of CO_2 ice-covered and ice-free regions within field of view (FOV). The TES spectrometer on board MGS observed such a relatively warm and bright ring lagging a few degrees of latitude behind the receding boundary of regions at CO_2 sublimation temperature, interpreted as H_2O frost [*Kieffer and Titus*, 2001]. *Wagstaff et al.* [2008] processed data from Thermal Emission Imaging System (THEMIS) spectrometer to monitor the spatial distribution of this moderately cold annulus during northern spring. However, *Kieffer and Titus* [2001] already pointed out that an unambiguous identification of ices in seasonal deposits required investigations in the near-IR (1 to 5 μm), as both H_2O ice and CO_2 ice present strong diagnostic absorption bands in this spectral range.

[6] The OMEGA imaging spectrometer aboard Mars Express covers a spectral range from 0.36 μm to 5.09 μm, extending from the visible across the near infrared, with a spectral resolution varying from 14 to 23 nm. The instantaneous field of view of OMEGA varies from less than 300 m at periapsis to several kilometers depending on the position of the Mars Express spacecraft on its elliptical orbit [*Bibring et al.*, 2004]. Strong distinct signatures of H_2O ice and CO_2 ice (Figure 1) with major absorption bands at 1.25, 1.5, 2, and 3 μm (H_2O ice) and 1.435, 2.281, 2.7, and 3.3 μm (CO_2 ice) [*Grundy and Schmitt*, 1998; *Quirico and Schmitt*, 1997; *Hansen*, 2005] are measured throughout images at different resolution. Therefore, the OMEGA instrument has the capability of unambiguously identifying and monitoring the abundance, physical state, distribution and temporal evolution of the CO_2, H_2O and dust components of the Martian frosts and ices. For instance, the composition of the seasonal deposits can be determined precisely, i.e., CO_2 ice with minor inclusions of water ice and dust [*Schmitt et al.*, 2005] and the presence of a CO_2-free water ice annulus lagging a few degrees behind the receding CO_2-rich condensates is confirmed [*Bibring et al.*, 2005]. This information is of prime importance for the understanding of the microphysics and the thermodynamics (radiative equilibrium) of the sublimation/condensation/deposition processes of volatiles. The TES instrument has shown that a large amount of water is released in the atmosphere during northern spring while CO_2 frost is sublimating, then continuing during part of the summer season [*Smith*, 2004; *Pankine et al.*, 2010]. An important question is the identification of the water vapor sources (seasonal deposits, permanent cap, regolith, etc.) as well as their relative contributions. The spatial distribution and absolute abundance of the deposits and their seasonal evolution provides strong constraints on the seasonal cycle of volatile exchange (mainly sublimation/condensation fluxes of CO_2 and H_2O) between the surface and the atmosphere. The abundance of dust within CO_2 or H_2O ices should also constrain the codeposition processes occurring during fall and winter. All of these data should also provide some clues to understand the current and past climatic cycles through the study of interannual evolutions.

[7] The organization of this paper is as follows. In section 2 we describe the OMEGA observations used in this study and the spectral parameters selected to monitor the seasonal deposits. Then in section 3 we present maps of the spatial distribution of both CO_2 and H_2O ices until complete disappearance of CO_2 ice. We analyze the boundaries of the seasonal deposits in terms of albedo, CO_2 ice, and H_2O ice, comparing OMEGA observations with MOC, TES, and THEMIS results. We also propose an interpretation for the early disappearance of the CO_2 ice spectral signature. Finally, in section 4 we present a possible scenario depicting the winter and spring evolution of the northern seasonal deposits and discuss the implications of these results.

2. OMEGA Observations and Relevant Parameters

2.1. OMEGA Observations

[8] Since January 2004, the OMEGA instrument has monitored three complete retreats of the northern seasonal

deposits. The present contribution is focused on the 2006 retreat, corresponding to MY 27 winter and MY 28 spring. The 2006 retreat will be called MY 27–28 retreat in the rest of the article. Northern seasonal deposits monitored during previous Martian years began receding near L_s 320° [*Kieffer and Titus*, 2001]. The OMEGA instrument has observed the seasonal deposits as soon as L_s 280°, just after winter solstice. These early observations correspond to the maximum extent of the seasonal deposits. We selected observations until L_s 95°, just after the summer solstice. After L_s 95°, seasonal frost is confined on the north permanent cap and disappears during summer [*Langevin et al.*, 2007]. A large number (1060) of OMEGA observations with adequate S/N ratio have been selected to follow the MY 27–28 retreat of the northern seasonal deposits.

2.2. Relevant Spectral Parameters for Seasonal Deposits Monitoring

2.2.1. Reflectance at 1.08 μm

[9] The seasonal deposits were first detected on the basis of their high albedo. MOC, TES and MARCI instruments monitored the albedo of the deposits from MY 24 to 29 [*James and Cantor*, 2001; *Benson and James*, 2005; *Kieffer and Titus*, 2001; *Cantor et al.*, 2010]. It is therefore important to monitor the albedo so as to compare the MY 27–28 OMEGA observations with previous observations. The albedo retrieved from MOC, TES, and MARCI measurements corresponds to a reflectance factor (RF), i.e., the ratio of the observed radiance to the incoming solar flux per unit of surface:

$$\text{RF}(\lambda) = \frac{I(\lambda)}{F_{\text{Sun}}(\lambda)\cos(\theta_i)}$$

where I(λ) is the radiance measured by the sensor, $F_{\text{Sun}}(\lambda)$ is the solar flux at the top of the atmosphere, and θ_i is the incident zenith angle. This reflectance factor was monitored in a 575–625 nm band pass by MOC [*James and Cantor*, 2001], by a visible/near IR bolometer (0.3 to 2.9 μm) on TES [*Kieffer and Titus*, 2001; *Christensen et al.*, 2001] and in seven bands centered between 258 nm and 718 nm by MARCI [*Cantor et al.*, 2010]. The OMEGA spectral range extending from 0.36 μm to 5.09 μm is covered by a visible channel and two IR channels [*Bibring et al.*, 2004]. We monitored the albedo in the low-wavelength IR channel instead of the visible channel for two reasons: the visible channel spatial resolution is lower than the IR channels spatial resolution and aerosol scattering decreases with increasing wavelength. The spectel at 1.08 μm located in the continuum was chosen. This spectel was used by *Langevin et al.* [2007] for its high S/N ratio to study the evolution of the southern seasonal deposits. The reflectance of pure ices is expected to have high albedo for small-grained frost across the visible and near IR. Therefore, the main differences observed between albedo at ~0.6 μm (MOC) and 1.08 μm (OMEGA) should result from the larger aerosol contributions in the visible. Relative variations of albedo with time as observed by OMEGA, MOC, TES, and MARCI can directly be compared.

[10] The reflectance factor does not depend on lighting and observing geometries for a perfect Lambertian surface.

However, ices and snow do not behave as Lambertian reflectors [*Li et al.*, 2007; *Warren*, 1982; *Dumont et al.*, 2010]. Specular reflection can occur for slab ices. The albedo of snow, i.e., hemispherical reflectance, increases with incidence angle. A strong forward scattering peak is another non-Lambertian effect observed for terrestrial snow [*Dumont et al.*, 2010]. If reflectance factor variations are observed in the OMEGA data set, it is therefore important to distinguish between photometric effects and changes induced by surface modification. Furthermore, aerosol extinction and scattering can have a significant effect on albedo as northern polar regions are observed at high incidence angles. In particular, albedo of bright surfaces such as ices is moderated by aerosols and spectral contrast is lowered [*Vincendon et al.*, 2007]. The impact of aerosols and photometric effects is discussed in section 2.2.4.

2.2.2. CO$_2$ Ice

[11] CO$_2$ ice is the main component of both northern and southern seasonal deposits. Several CO$_2$ ice absorption bands are available in the OMEGA spectral range (Figure 1). The narrow 1.435 μm absorption band provides the best S/N ratio among the CO$_2$ ice bands which do not saturate, except for path lengths greater than 20 cm. Therefore this absorption band was used by *Langevin et al.* [2007] to study the evolution of the southern seasonal deposits. We use this same band to probe CO$_2$ ice. This absorption band lies very close to a minor absorption feature of atmospheric CO$_2$, at 1.443 μm. It is also overlapped by the short-wavelength wing of the broad 1.5 μm absorption feature of H$_2$O ice which extends from 1.38 μm to 1.8 μm (Figure 1). *Langevin et al.* [2007] used the spectel at 1.429 μm, the closest to the bottom of this band and near the optimum of the photometric function of OMEGA. They developed a specific CO$_2$ band depth evaluator for the OMEGA data so as to minimize the impact of these absorption features:

$$R_{\text{CO}_2} = \frac{\text{RF}(1.429\ \mu\text{m})}{\text{RF}(1.385\ \mu\text{m})^{0.5} \times \text{RF}(1.443\ \mu\text{m})^{0.5}}$$

The baseline spectel at 1.385 μm is located outside the wide 1.5 μm absorption band of H$_2$O ice while the baseline spectel at 1.443 μm lies within the short-wavelength wing of this H$_2$O ice absorption band. R_{CO_2} is a reflectance ratio, $(1 - R_{\text{CO}_2})$ is then dimensionally equivalent to a band strength. $(1 - R_{\text{CO}_2})$ is very close to 0 for modeled and observed spectra of pure H$_2$O ice so that large admixtures of H$_2$O frost have only a small impact on this evaluator. Since the baseline spectel at 1.443 μm is located within the H$_2$O ice absorption band, $(1 - R_{\text{CO}_2})$ underestimates the strength of the CO$_2$ ice band. We evaluate the band strength by comparing spectra of two regions located at similar altitudes, so as to have the same absorption by atmospheric CO$_2$ at 1.443 μm. In the first region, spectra exhibit both CO$_2$ and H$_2$O signatures. In the second region, spectra have been chosen to exhibit the same H$_2$O ice band strength at 1.5 μm as in the first region but without CO$_2$ ice signature (Figure 2). We assume that the mixing of atmospheric and ices signature is multiplicative. By dividing these two spectra, we delete the effect of both the H$_2$O ice band and the 1.443 μm atmospheric band. We thus obtain an undisturbed band
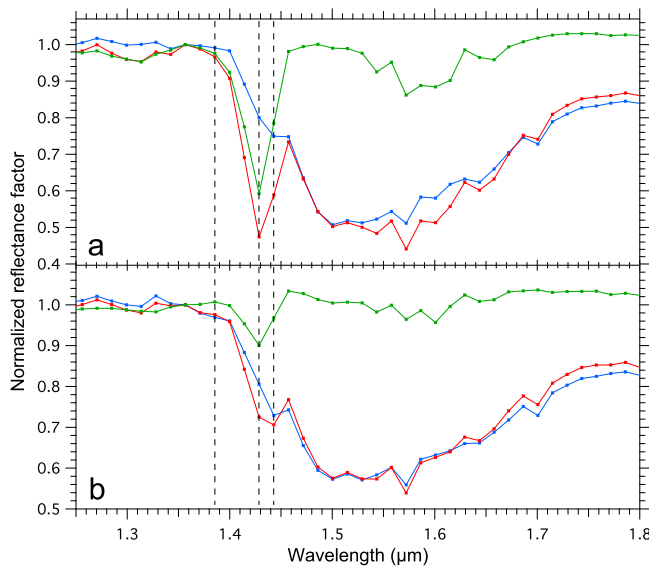
Figure 2. Evaluation of the CO_2 ice band strength at 1.429 μm. (a) Red spectrum taken on a region covered by CO2 ice including low content of H_2O ice and (b) red spectrum taken on a region covered by CO_2 ice including a relatively high content of H_2O ice. The red spectra exhibit both CO_2 and H_2O ice absorption bands, whereas the blue spectra exhibit no CO_2 ice signatures but the same H_2O ice band strength at 1.500 μm as in the red spectra. Red spectra differ from each other by the degree of H_2O ice content. Red and blue spectra are taken in regions located roughly at the same altitude so as to have the same absorption by atmospheric CO_2 at 1.443 μm. Both spectra are normalized to the reflectance value at 1.357 μm. Green spectra are obtained by dividing the red spectrum by the corresponding blue spectrum. They provide an estimate of the CO_2 ice band strength at 1.429 μm: 0.408 for the region of Figure 2a and 0.120 for the region of Figure 2b. These estimates are very consistent with the values provided by the BD_{CO2} (1.429 μm) evaluator when applied on the red spectra: 0.410 for Figure 2a and 0.110 for Figure 2b. Dashed lines indicate the position of spectels used for this evaluation.

led to the following evaluator for the strength of the CO_2 ice band at 1.429 μm (see Figure 3) (BD, band depth):

$$BD_{CO_2}(1.429 \ \mu m) = 1.225(1 - R_{CO_2}) - 0.044$$

We estimate the uncertainty on the determination of this band depth to ±0.01 reflectance unit.

2.2.3. H_2O ice

[12] The presence of area of H_2O ice in the northern seasonal deposits has been inferred by TES temperature measurements [*Kieffer and Titus*, 2001] on the basis of its temperature intermediate between that of CO_2 ice (150 K) and defrosted dust (>220 K). It was then directly detected by the OMEGA instrument [*Schmitt et al.*, 2005]. H_2O ice has several broad absorption bands in the OMEGA spectral range. The strongest bands are located at wavelengths of 1.5 μm, 2 μm and 3 μm (Figure 1). The 3 μm absorption band saturates when the path length of photons within H_2O ice exceeds a few μm. Longer paths are required for the 2 μm band (a few hundred μm) and the 1.5 μm band (~1 mm) [*Grundy and Schmitt*, 1998]. The grain sizes for H_2O ice on the surface ranges between a few tens of μm (frost) and about 1 mm (perennial northern ice cap) [*Langevin et al.*, 2005]. Therefore the 3 μm band is not best suited to monitor the texture of surface ice, while it is a sensitive indicator for minerals hydration [*Jouglet et al.*, 2007; *Milliken et al.*, 2007; *Pommerol and Schmitt*, 2008a, 2008b]. At wavelengths around 2 μm, there are strong CO_2 absorption features both in the solid state (Figure 1) and in the atmosphere. Therefore the 1.5 μm band is clearly best suited to monitor H_2O ice on the surface with OMEGA. This spectral range provides optimum S/N [*Langevin et al.*, 2007]. It saturates only for very large grain sizes which are not expected for surface frost, and there are only weak CO_2 absorptions from either ice or gas at the center of the band (Figure 1). We used the evaluator developed by *Langevin et al.* [2007]. They compared the reflectance factor at 1.5 μm to a continuum evaluated from the reflectance factor at two OMEGA wavelengths 1.385 μm and 1.772 μm away from major CO_2 and H_2O absorption bands, taking into account the intervals

strength of the CO_2 ice at 1.429 μm. We did this work for 8 different CO_2 ice band strengths. We also evaluated the mean value of $(1 - R_{CO2})$ for regions not covered by CO_2 ice but still exhibiting the 1.5 μm H_2O ice absorption band. An analysis of spectra and latitudinal profiles of both $(1 - R_{CO2})$ and the H_2O ice signature has been done at several steps of the seasonal deposits retreat. It indicates that for the vast majority of observations no CO_2 ice signature is observed for H_2O ice signature at 1.5 μm lower than 0.15. $(1 - R_{CO2})$ takes small fluctuating values on defrosted regions, probably because of varying surface dust spectra or modification of the optical depth of atmospheric dust. These values are not relevant; only $(1 - R_{CO2})$ values where the H_2O ice signature is higher than 0.05 are considered. We therefore defined the CO_2 zero level as the average of $(1 - R_{CO2})$ on regions where the H_2O ice signature ranges from 0.05 to 0.15. The correlation between the undisturbed band strengths and the corresponding values of $(1 - R_{CO2})$
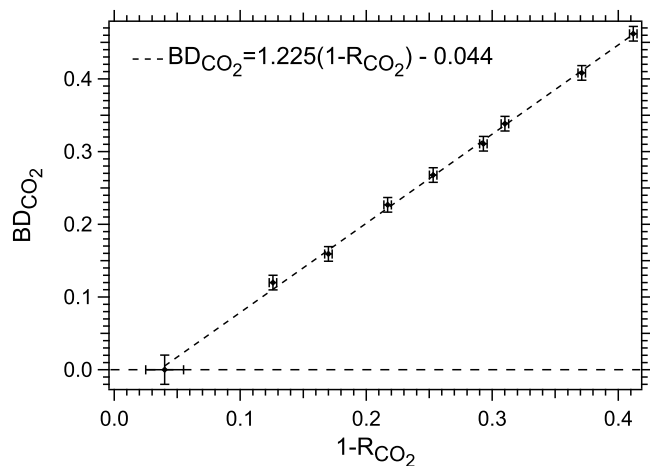

Figure 3. Correlation between the undisturbed band strengths BD_{CO2} (1.429 μm) and the corresponding values of $(1 - R_{CO2})$.

between the center of the band and the selected continuum regions:

$$\mathrm{BD}_{H_2O}(1.500~\mu m) = 1 - \frac{\mathrm{RF}(1.500~\mu m)}{\mathrm{RF}(1.385~\mu m)^{0.7} \times \mathrm{RF}(1.772~\mu m)^{0.3}}$$

We estimate the uncertainty on the determination of this band depth to ±0.005 reflectance unit.

[13] An instrumental problem was identified in the observation mode of OMEGA with the largest swath (128 pixels), with one out of two lines being perturbed for columns 81 to 96 after orbit 511. This problem extended to columns 65 to 128 after orbit 2124. In these parts of the image cubes, the corrupted observations were replaced by the average of the uncorrupted previous and next lines. However, the correction on spectels used in both the CO_2 and H_2O ice absorption strength evaluators is not fully reliable. Therefore, while still containing interesting information for mapping purposes (in particular for the albedo at 1.08 μm), the last 64 columns of 128 columns mode images have to be considered with caution and they cannot be used for spectral modeling purposes.

2.2.4. Impact of Aerosols and Ice Photometric Effects on Reflectance and Band Strengths

[14] Northern polar regions can only be observed at relatively high incidence angles, particularly close to spring equinox with incidence angles higher than 80°. Aerosol extinction and scattering are a major factor for such geometries, even at low optical thickness conditions. Moreover, the large latitudinal extension of the seasonal deposits at the beginning of spring results in incidence angle variations of more than 30°. It is therefore important to assess the impact of atmospheric dust on the observed albedo and ices band depths before concluding on a surface modification. In order to estimate this impact, we studied the influence of illumination geometry for a 13 km^2 homogeneous region located on Rupes Tenuis. We selected two successive observations of this area acquired in nadir pointing mode at two different incidence angles, 60.1° and 68.6°. The region is covered by bright seasonal frost at the time of observations (L_s ~67°). We observe a 12% decrease of the reflectance factor at 1.08 μm and a 12% decrease of the H_2O ice band depth at 1.5 μm when incidence angle increases, i.e., when solar photons encounter a higher quantity of aerosols. The variation of the CO_2 ice band depth at 1.43 μm is within uncertainty on band depth determination. As expected, aerosol extinction and scattering lower the albedo of this bright region and reduce the spectral contrast [Vincendon et al., 2007].

[15] Correcting the aerosol impact for the entire data set is not straightforward. As discussed by Vincendon et al. [2007], it can only be performed on regions which are observed at close intervals with two different geometries. Even then, it relies on the assumption that there is no variation of both the aerosol optical thickness and the surface between the observations. If there is only one geometry of observation available, the optical thickness of aerosols can still be determined provided some CO_2 ice bands show saturation such as the ones at 2.01 or 2.64 μm. Such a method has been applied for observations of the southern seasonal deposits [Langevin et al., 2007] but it is not applicable for the northern

seasonal deposits where no saturated CO_2 ice band are observed. We decided, as a first step, to present the time sequences of mosaics without correction of aerosol effects. The overall self-consistency of the mosaics at overlaps between swaths at different incidence angles demonstrates that this approach provides a sound basis for studying the winter and spring retreat of the northern seasonal deposits.

[16] Ice reflectance and band depths can also depend on the emission angle due to a combination between photometric effects of the ice and aerosol scattering. Most of OMEGA observations used in this study are obtained with nadir pointing. For a single 128 columns image, the emission angle varies from 0° to 10°, with only a minor impact of non-Lambertian behavior and aerosols. Nevertheless, some observations were acquired in inertial mode between L_s 350° and L_s 66°. In this mode, the emission angle varies from 0° to 90°. The part of the image where emission angle is higher than 55° is undersampled and entails problems of projection. For such off-nadir observations, we therefore only considered pixels for which the emission angle is lower than 55°. In order to assess the impact of non-Lambertian behavior and aerosols for emission angles lower than 55°, we studied a 13 km^2 homogeneous region located on Olympia Planitia. We selected two successive observations of this area acquired with an incidence angle of ~65° at two different emission angles, 0.7° and 45.1° The azimuth angle of the second observation is 106°. Bright seasonal frost covers the region at the time of observations (L_s ~51°). We observe a 14% increase of the reflectance factor at 1.08 μm and a 9% decrease of the H_2O ice band depth at 1.5 μm when emission angle increases. The variation of the CO_2 ice band depth at 1.43 μm is within uncertainty on band depth determination. It is known that the phase function of Martian aerosols is strongly forward scattering [Ockert-Bell et al., 1997]. Since the azimuth of the off-nadir observation is higher than 90°, the reflectance increase observed for increasing emission angle could therefore be explained by the increase of the path radiance of the aerosols. However, surface ice also behaves as a non-Lambertian reflector with a strong forward scattering peak [Dumont et al., 2010]. The reflectance increase is thus likely due to a combination of both aerosols and ice photometric effects. Interestingly, Cantor et al. [2010] observe similar reflectance increase for increasing emission angles while monitoring a region of the residual north polar cap in summer (L_s ~134°). They mention that the ranges of incidence and phase angles during these observations are very small; we can deduce that the azimuth of their off-nadir observations is close to 90°, thus comparable to the 106° azimuth of our off-nadir observation. For similar geometry of observation, Cantor et al. [2010] therefore observe similar reflectance variations in spite of the different nature of the ice covering the permanent cap (CO_2 ice in spring, H_2O ice in summer) and a different aerosol optical depth.

[17] In the literature, a Henyey-Greenstein phase function with an asymmetry parameter of 0.63 is commonly chosen for aerosols [Ockert-Bell et al., 1997]. On the contrary, the seasonal frost phase function is unknown. If the optical depth of aerosols was known, then the phase function of the frost could be retrieved. But the lack of saturated CO_2 ice band and the restricted geometries of observation prevent the determination of the aerosol opacity. Therefore, it is not
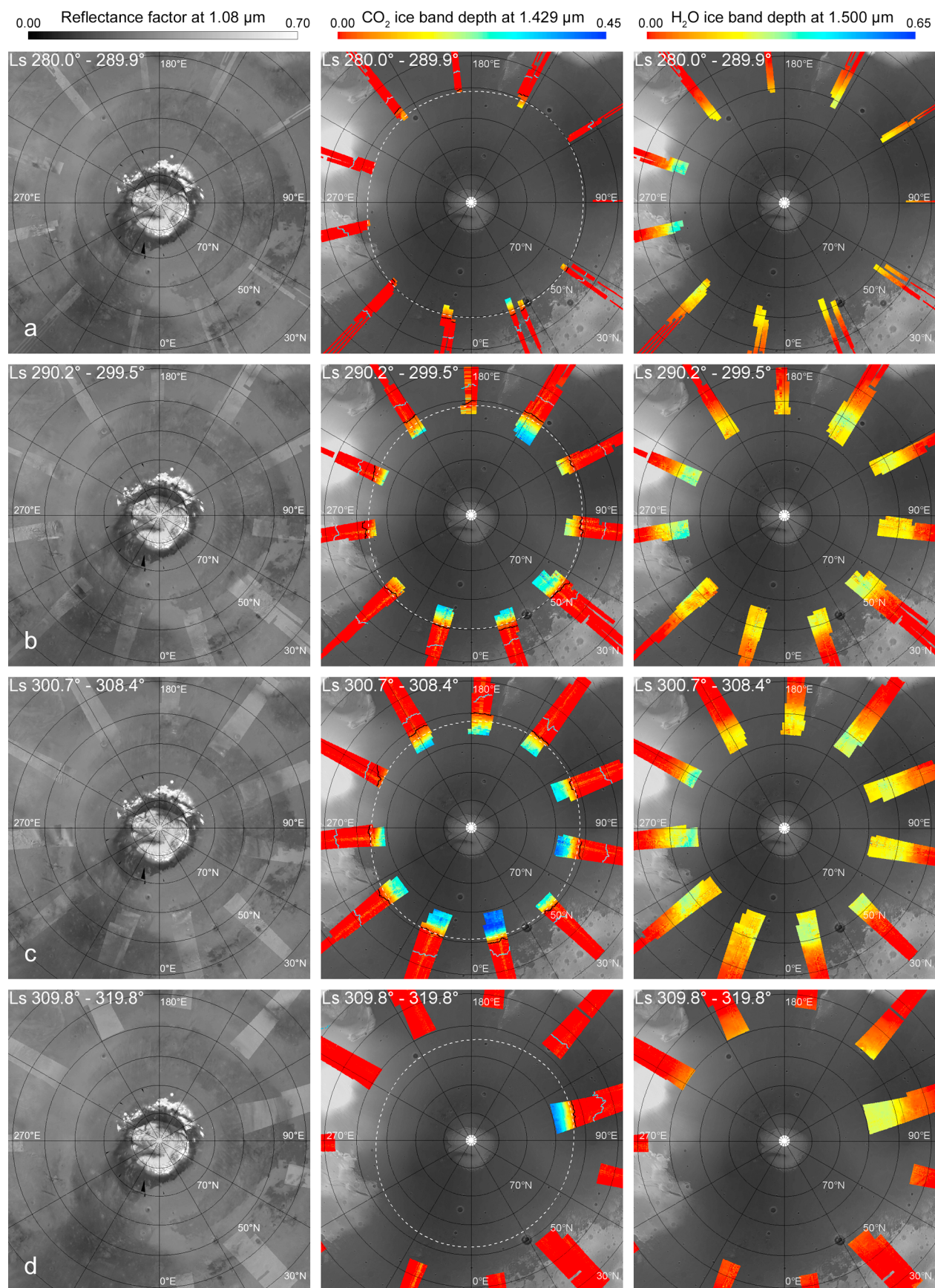
Figure 4

possible at this stage of the analysis to separate aerosols and surface effects for high emission angles. Most of the geometries of observation are generally not so extreme. As previously explained, the overall self-consistency of the mosaics demonstrates that reflectance and band depths variations are primarily due to surface modification. However, every time a significant variation of these spectral parameters is observed, we checked whether it is correlated with changes in lighting or observing geometries before concluding on a surface effect.

3. Temporal Evolution of the Spatial Distribution of CO_2 and H_2O Ices

[18] The three selected evaluators (reflectance factor at 1.08 μm, CO_2 ice absorption strength at 1.429 μm, H_2O ice absorption strength at 1.5 μm) have been calculated for the whole OMEGA data set between L_s 280° and 95° and above 30°N latitude and then mosaiced into north polar stereographic projection to create temporal maps spanning 0.4 to 10° L_s depending on the density of observations. These maps are presented in Figures 4–9. Three boundaries have been added on these mosaics: the TES "crocus line" [Kieffer and Titus, 2001], the OMEGA CO_2 ice boundary and the OMEGA H_2O ice boundary. Procedures used to retrieve these boundaries are described below.

[19] It is important to note that an ice absorption band depth is related to the total quantity of ice present on the surface only if that ice is optically thin at the band wavelength. If ice is optically thick, the band depth will strongly depend on the way the ices and dust are mixed at the pixel scale, and it will be correlated to the relative proportion between each constituent of a granular mixture, but it is also dependent on the mean ice grain size. Thus the band depth maps mostly provide a qualitative information on the repartition of both CO_2 and H_2O ices but, in most cases, neither on the depth nor on the total amount of ice covering the Martian soil. In the rest of this paper, CO_2 and H_2O ice absorption band depth maps will be simply called CO_2 and H_2O ice maps. Maps of the reflectance factor at 1.08 μm will be called albedo maps.

3.1. General Description of the Maps

[20] Sections 3.1.1–3.1.3 give a general description of the northern seasonal deposits evolution in term of albedo, CO_2 ice coverage, and H_2O ice coverage.

3.1.1. Albedo Maps

[21] From L_s 280° to L_s 340° (Figures 4a to 5b), seasonal deposits are seen on both CO_2 and H_2O ice maps but not on albedo maps. For a single OMEGA observation, no albedo contrast is observed at the transition between bare defrosted soil and soil covered by frost. This surprising configuration

is shown on Figure 10. The distribution of the CO_2 ice band depth is shown on Figure 10a. Regions located north of 50°N are covered by CO_2-rich ice while southern regions are not. No albedo transition is observed between these two regions on Figure 10b. Furthermore, known albedo features observed in summer on the Vastitas Borealis plains showing sharp transition between bright and dark soil are still observed in winter even on regions covered by frost. Figure 10c corresponds to MOC albedo data acquired in summer, taken from the MOC wide-angle image atlas [Caplinger and Malin, 2001]. An albedo transition is observed at ~54°N. This albedo transition is still observed in winter even with a frost coverage (Figure 10b). These characteristics tend to prove that winter northern frost is either transparent at 1 μm or spatially segregated at subpixel scale with bare defrosted soil. If ice is spatially segregated with defrosted soil, then we would expect that more and more surface is covered by ice with increasing latitude. Then for a soil with a given summer albedo, the winter albedo should increase with latitude. It is not observed on Figure 10b on regions north 55°N. Therefore the most likely explanation is that winter frost is transparent at 1 μm. One can argue that the two data sets are not comparable since this MOC albedo mosaic is made with the reflectance factor at 600 nm whereas OMEGA mosaics are done at 1 μm. Therefore we also retrieved the 603 nm reflectance factor mosaics from the OMEGA visible channel observations. Comparison between the OMEGA mosaics acquired at 603 nm and at 1 μm shows that for both mosaics no albedo contrast is observed at the transition between bare defrosted soil and soil covered by frost. The comparison between MOC and OMEGA mosaics is thus valid.

[22] Transparent frost is observed until L_s 329°. Between L_s 329° and L_s 349°, regions covered by CO_2 ice have not been monitored by the OMEGA instrument. On the next OMEGA observation, at L_s 350°, all the surface covered by CO_2-rich seasonal frost appears brighter than bare defrosted soil (Figure 5c). This demonstrates that a change in the optical properties of the CO_2 frost has occurred between L_s 329° and L_s 350°. A MOC mosaic acquired during MY 24 at L_s 343° clearly shows an albedo transition between surface covered by frost and defrosted soil [see James and Cantor, 2001, Figure 1a]. The frost physical state modification therefore occurs between L_s 329° and L_s 343° assuming no interannual variability between MY 24 and MY 27, an assumption supported by multiyear observations [e.g., Titus, 2009].

[23] From L_s 350° to L_s 95°, the seasonal deposits evolution in term of albedo is mostly the same as that observed by James and Cantor [2001], Kieffer and Titus [2001], and Benson and James [2005] in 2000 and 2002. At first glance,

Figure 4. Evolution of the northern seasonal deposits in terms of (left) reflectance factor at 1.08 μm, (middle) CO_2 ice band depth at 1.429 μm, and (right) H_2O ice band depth at 1.500 μm for four sets of observations: (a) L_s 280.0°–289.9°, (b) L_s 290.2°–299.5°, (c) L_s 300.7°–308.4°, (d) L_s 309.8°–319.8°. The OMEGA albedo maps are displayed over MOC albedo data acquired in summer [Caplinger and Malin, 2001] as a background. CO_2 ice and H_2O ice maps are displayed over MOLA topography as a background, with altitudes stretching between −5500 m and 3500 m [Zuber et al., 1998]. Three important boundaries are plotted on the CO_2 ice band depth map: the black outline corresponds to the OMEGA CO_2 ice boundary, the blue outline is the OMEGA H_2O ice boundary and the white dashed outline is the TES "crocus line" (limit of low temperatures compatible with surface CO_2 ice, averaged over 3 MY of TES observations) computed for the mean L_s of each L_s range.
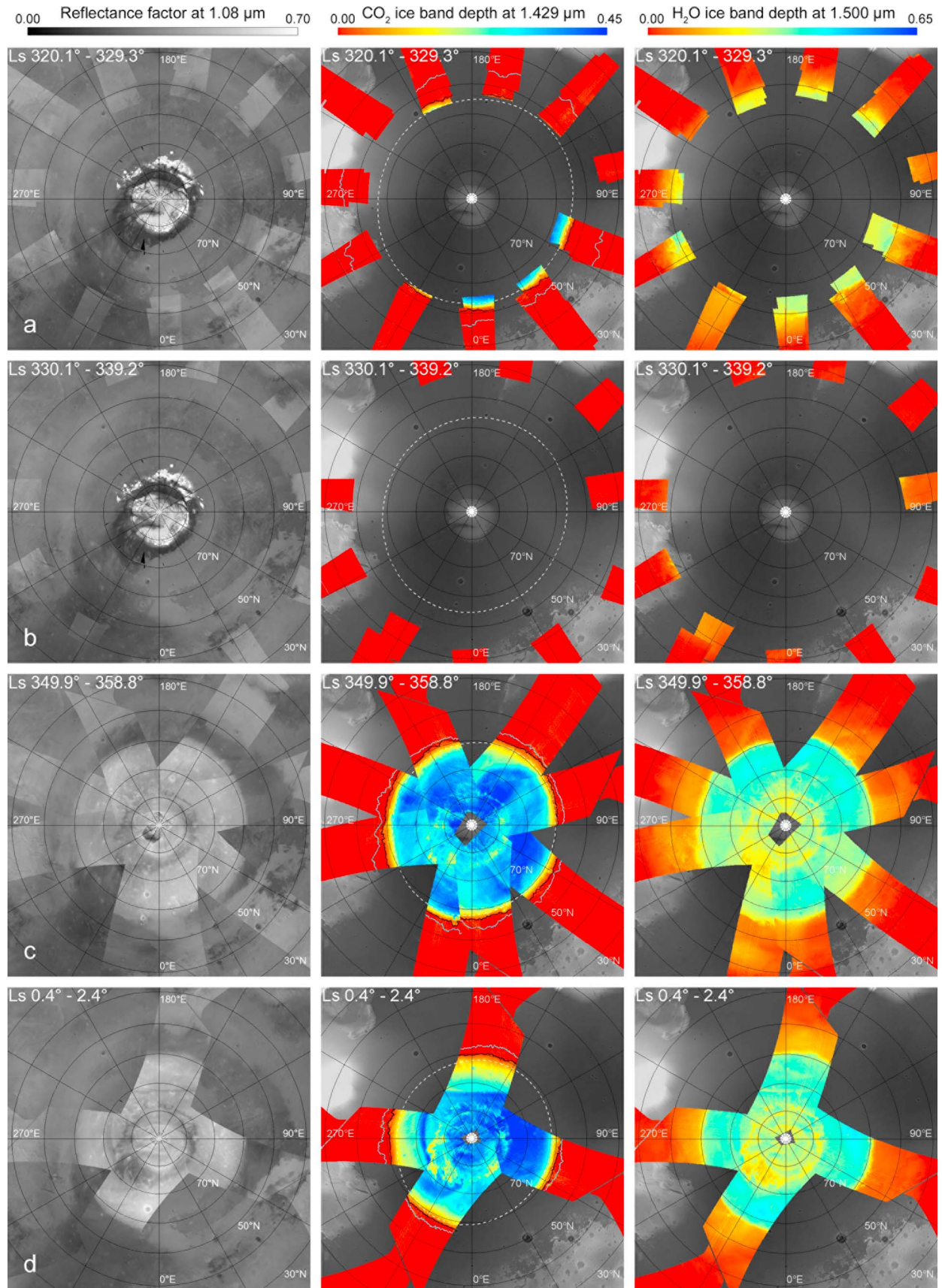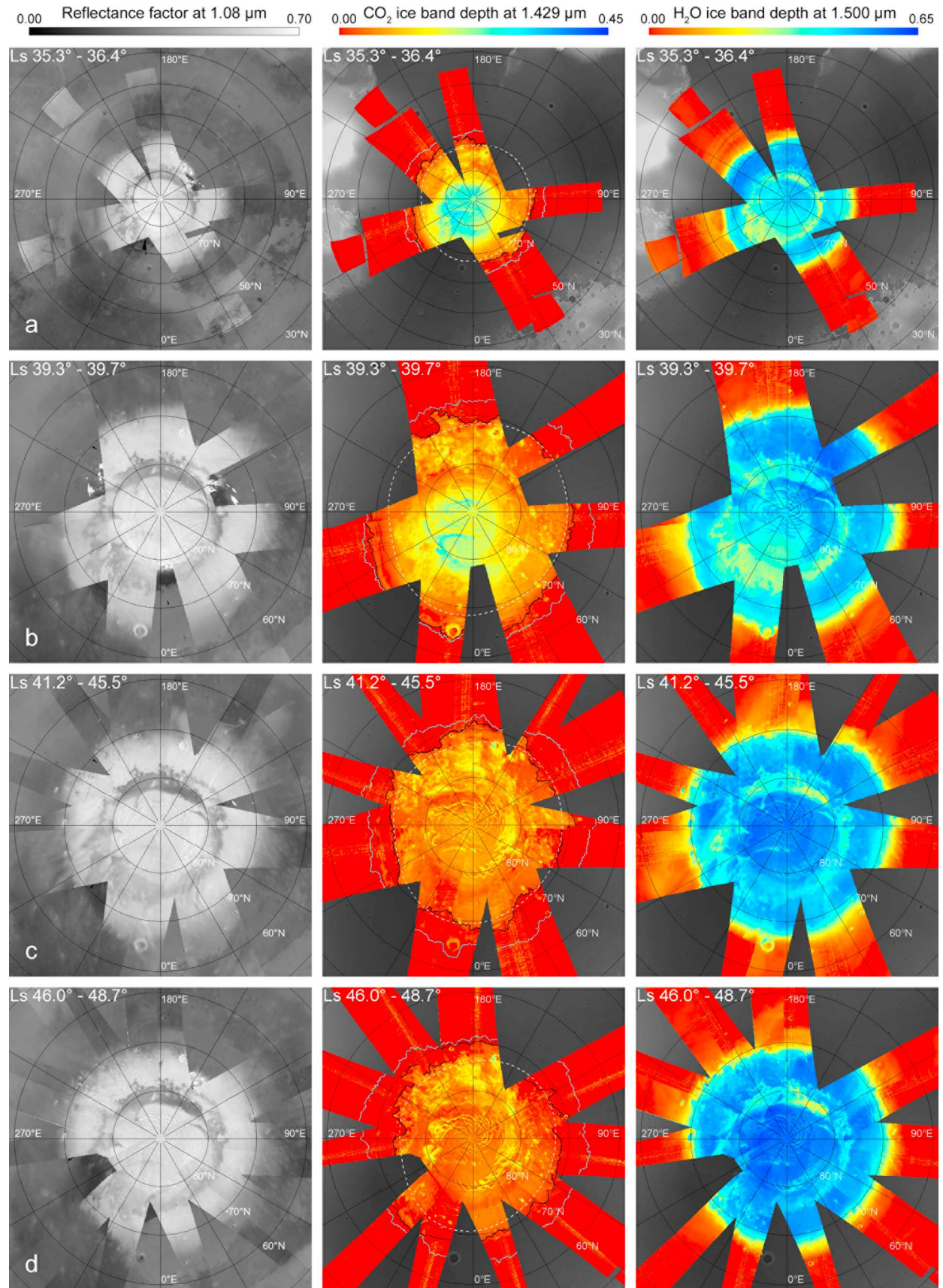
Figure 5. Same as Figure 4 but for (a) L_s 320.1°–329.3°, (b) L_s 330.1°–339.2°, (c) L_s 349.9°–358.8°, (d) L_s 0.4°–2.4°.
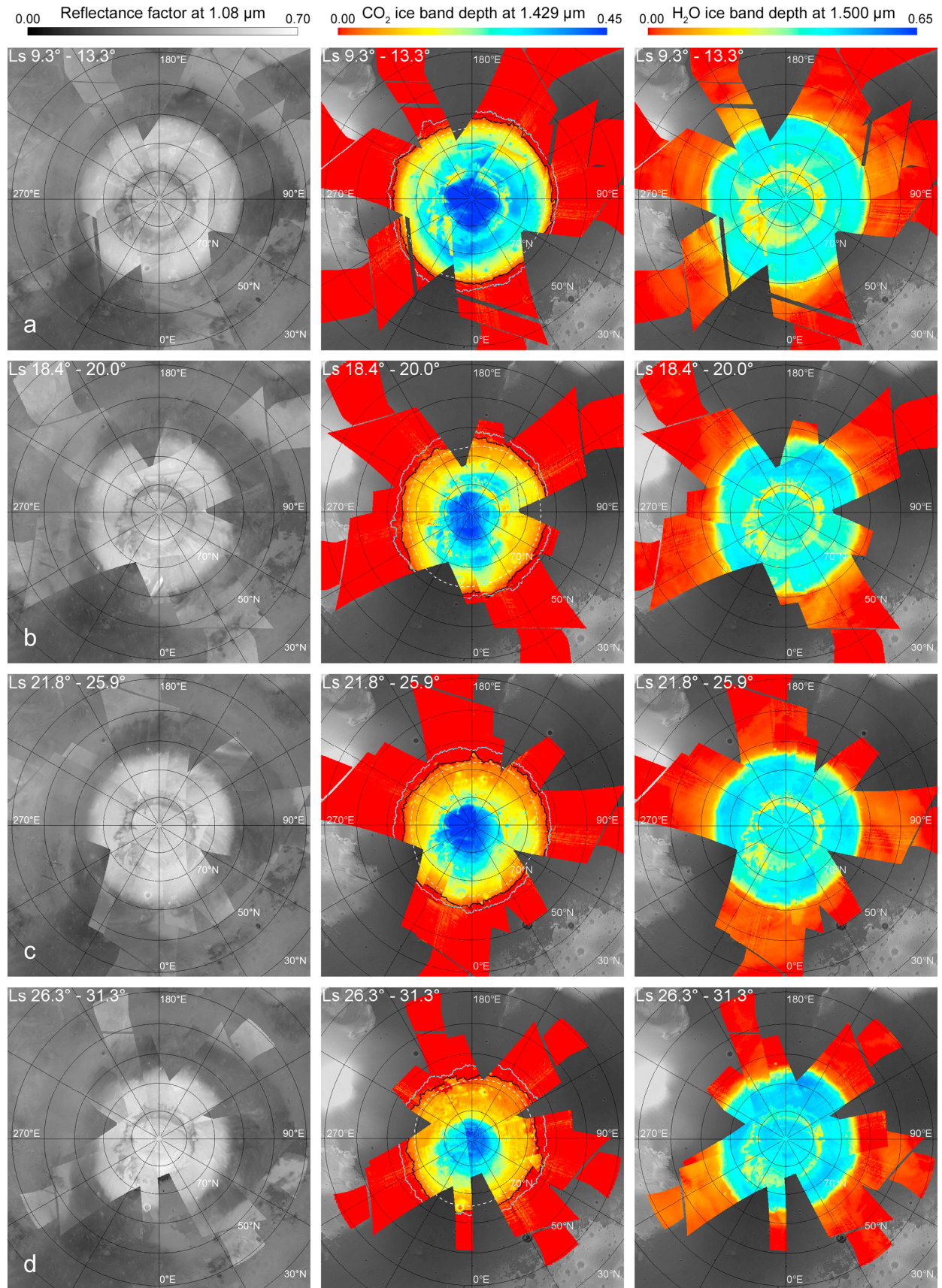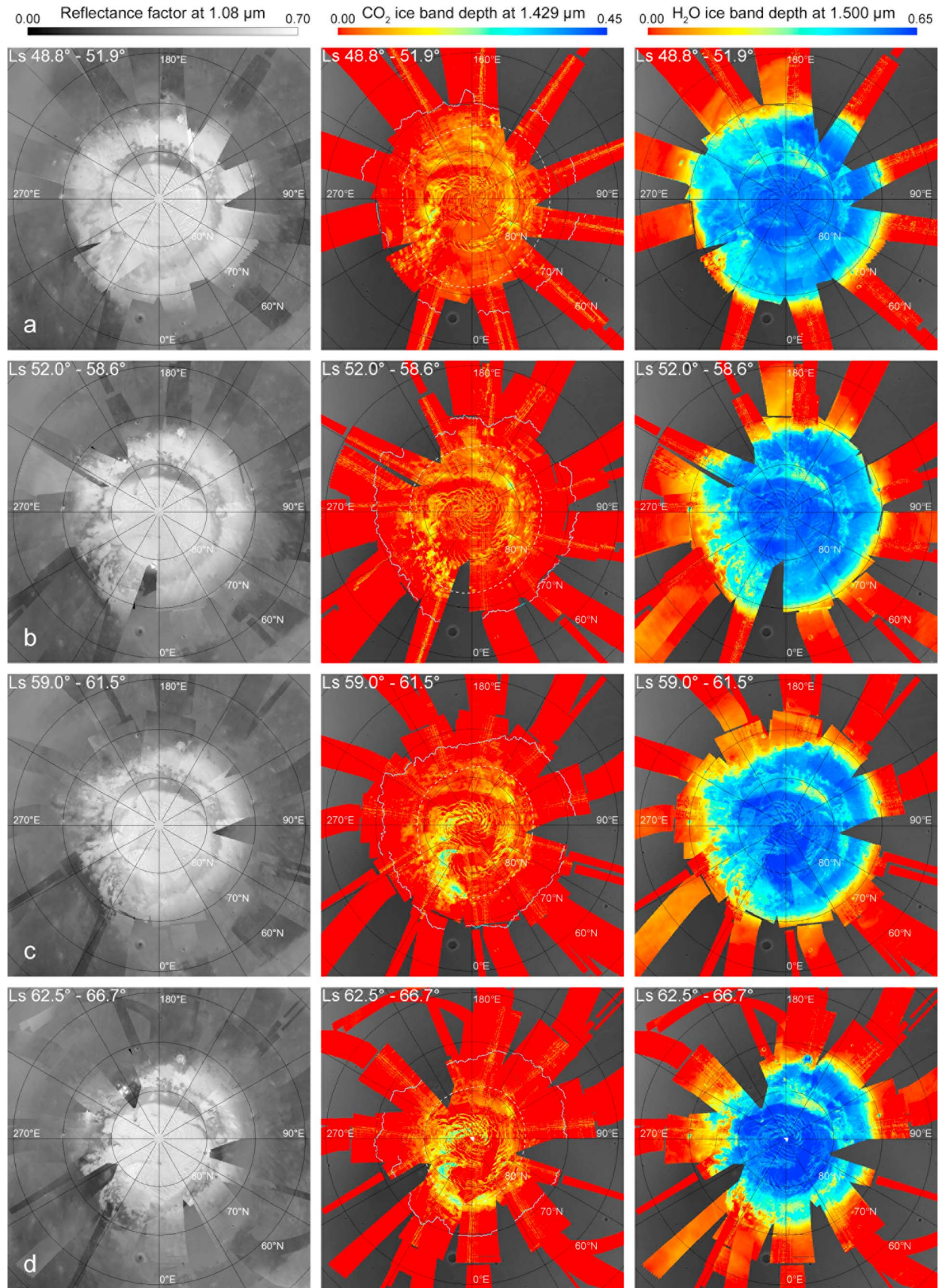
Figure 6. Same as Figure 4 but for (a) L_s 9.3°–13.3°, (b) L_s 18.4°–20.0°, (c) L_s 21.8°–25.9°, (d) L_s 26.3°–31.3°.
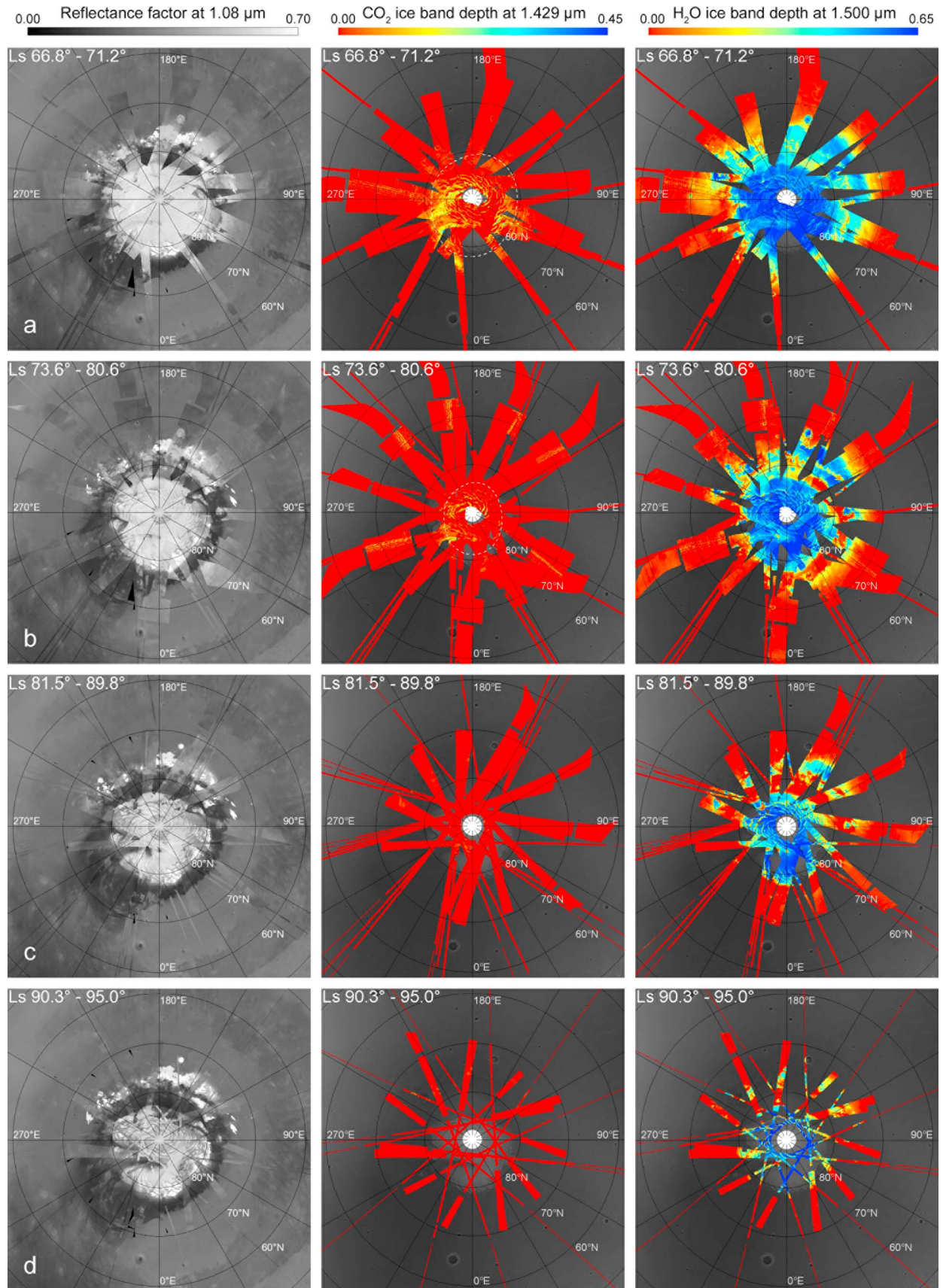
Figure 7. Same as Figure 4 but for (a) L_s 35.3°–36.4°, (b) L_s 39.3°–39.7°, (c) L_s 41.2°–45.5°, (d) L_s 46.0°–48.7°.
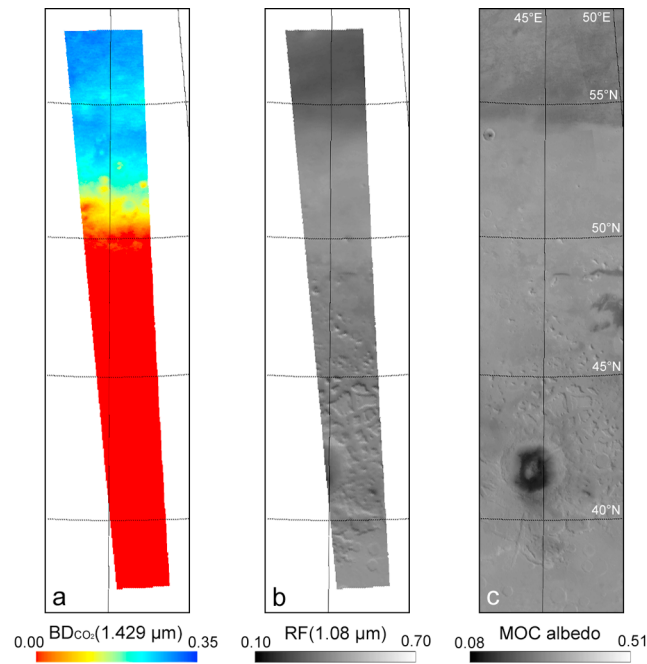
Figure 8. Same as Figure 4 but for (a) L_s 48.8°–51.9°, (b) L_s 52.0°–58.6°, (c) L_s 59.0°–61.5°, (d) L_s 62.5°–66.7°.

Figure 9. Same as Figure 4 but for (a) L_s 66.8°–71.2°, (b) L_s 73.6°–80.6°, (c) L_s 81.5°–89.8°, (d) L_s 90.3°–95.0°.

0.00 $BD_{CO_2}(1.429\ \mu m)$ 0.35 $\quad$ 0.10 $RF(1.08\ \mu m)$ 0.70 $\quad$ 0.08 MOC albedo 0.51

Figure 10. (a) The 1.429 μm CO_2 ice band depth for OMEGA observation 2210_7 (L_s 299.5°). (b) Reflectance factor (RF) at 1.08 μm for the same observation. (c) MOC albedo data acquired in summer [*Caplinger and Malin*, 2001]. No albedo contrast is observed at the transition between defrosted soil and soil covered by frost. The albedo transition observed in summer at ~54°N is still observed in winter with a weaker contrast, suggesting that winter frost is partly transparent at 1.08 μm.

it appears that the seasonal deposits are remarkably axisymmetric and uniform from L_s 350° to L_s 50° (Figures 5c to 7d). Departures from this uniformity are the circumpolar dark dunes field (also called polar erg) surrounding the permanent north polar cap, and some frost-rimmed craters and bright crater streaks extending counterclockwise from the crater. Crater streaks were also observed by MOC on the same longitudinal range, i.e., 210°E–300°E [*James and Cantor*, 2001], a sector which is known to be very active meteorologically with baroclinic wave activity [*Hollingsworth et al.*, 1995, 1996]. After L_s 350°, there is no tendency of known albedo features from the mineral soil to show up beneath the surface frost, supporting the fact that the frost is optically thick in the visible. The only exception is the polar erg which has a cryptic behavior, i.e., temperature near the CO_2 frost point and albedo almost as low as the underlying soil [*Kieffer et al.*, 2000]. TES albedo measurements indicated that the polar erg albedo is slightly higher in spring than in summer, suggesting that the frost covering the polar erg is not completely transparent [*Kieffer and Titus*, 2001]. *James and Cantor* [2001] reported that the albedo of the deposits at a fixed L_s increased from the polar cap toward the outer edge. They correlated this trend with the gradual increase of albedo with insolation that was observed in Viking data [*Paige*, 1985]. We do not observe such a trend on OMEGA mosaics.

[24] The northern seasonal deposits are much less symmetric between L_s 50° and 67° (Figures 8a–8d). The deposits exhibit a polygonal shape observed by MOC at L_s ~60° [*James and Cantor*, 2001] and already observed during previous northern Martian springs by the Hubble Space Telescope [*Cantor et al.*, 1998] and by the Mariner 9 probe [*Soderblom et al.*, 1973]. However, the seemingly straight boundaries connected by sharp angles observed by HST are resolved into a more irregular shape by OMEGA and MOC. Between L_s 62° and 67° (Figure 8d), the shape of the deposits is less polygonal but still irregular. After L_s 67° (Figure 9a), the geographic coverage of the OMEGA instrument is too small to enable a reliable analysis of the shape of the deposits.

[25] The albedo of the northern seasonal deposits increases during their retreat. This overall brightening as the Sun elevation increases was first noted by *Paige* [1985] and has also been observed during the 2000 and 2002 recessions by *James and Cantor* [2001]; *Kieffer and Titus* [2001]; *Cantor et al.* [1998]. Several processes have been proposed to explain this brightening: a decrease of the mean grain size combined with a decrease of the aerosols optical depth [*Langevin et al.*, 2007], a process progressively removing the dust from the ice [*Cantor et al.*, 1998] or a photometric behavior of the ices although this last phenomenon cannot fully explain the amplitude of albedo variation. This brightening is also observed for seasonal ices of the southern hemisphere and may be explained by self cleaning of the ice by solid-state greenhouse effect as discussed by *Kieffer* [2007] and *Portyankina et al.* [2010].

3.1.2. CO$_2$ Maps

[26] The monitoring of CO_2 and H_2O ices distributions provides a more detailed view of the deposits evolution. From L_s 280° to 350°, only the edge of the seasonal deposits is monitored (Figures 4a to 5b). After L_s 350°, we have access to a nearly full coverage of both ices distributions every degrees of L_s.

[27] The maximum extent of CO_2 ice is 49°N at L_s 289°. CO_2 ice distribution is mostly axisymmetric at the beginning of the recession. It becomes less and less axisymmetric from L_s 40° to L_s 50°. After L_s 50°, the distribution of CO_2 ice is more and more patchy until its complete disappearance at L_s ~80° (Figure 9c).

[28] The distribution of CO_2 ice band depths is not as uniform as that of the albedo. Strong spatial variations are observed between L_s 350° and 2.5° (Figures 5c and 5d). Linear structures observed near longitude 150°E at L_s 350° (Figure 5c) correspond most likely to circumpolar clouds. A weaker signature of CO_2 ice is observed on the circumpolar dark dunes field between L_s 350° and L_s 13° (Figures 5c to 6a). There is a general increase of CO_2 ice band depth toward the north polar cap for a given L_s, from L_s 10° to 40°. After L_s 40°, this behavior is no longer observed.

[29] Between L_s ~40° and L_s ~70°, the CO_2 ice signature unambiguously reappears at locations where it had previously disappeared. As an example, no CO_2 ice is detected at L_s 50° on a region located at 350°E/75°N (Figure 8a), while it is observed anew at L_s 60° (Figure 8c). This surprising behavior requires a specific discussion which is beyond the scope of this article and will be discussed in detail in a specific article. Despite these nonuniformities, the general
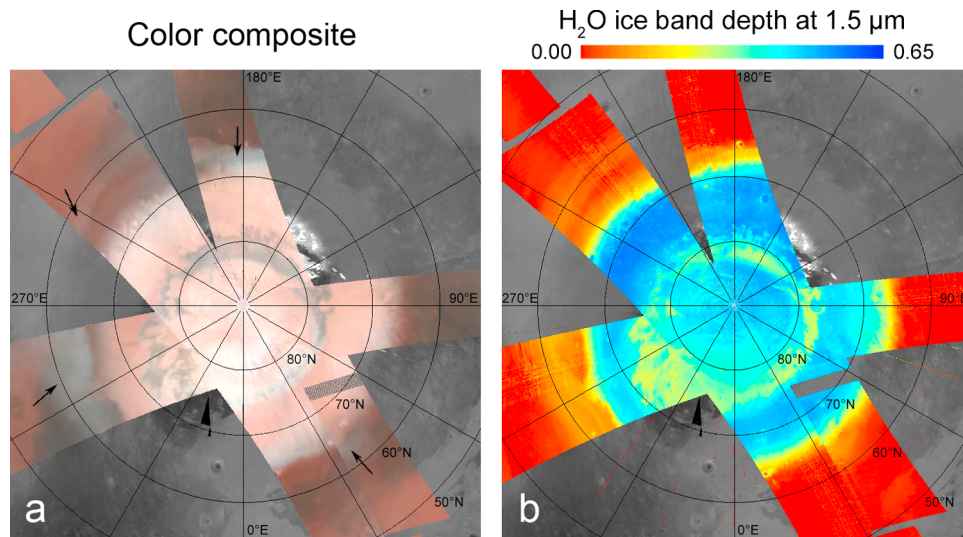
Figure 11. Comparison between (a) a color composite mosaic from the OMEGA visible channel and (b) a H_2O ice band depth mosaic, both acquired between L_s 35.3° and 36.4°. Spectels at 699.7, 535.9, and 476.0 nm were used for the red, green, and blue layers, respectively, of the RGB composite. Arrows point to water ice clouds extending beyond the boundary of the receding northern seasonal deposits. These clouds are also observed on the H_2O ice band depth mosaic, with band depths lower than 0.15 and a characteristically strong absorption at 3 μm.

trend is a decrease of the CO_2 ice band depth throughout the retreat of the seasonal deposits.

3.1.3. H$_2$O Maps

[30] The distribution of the H_2O ice can be divided into two main categories. The first one is an area seemingly fitting with the seasonal deposits distribution in term of albedo (e.g., Figure 5c). H_2O ice band depth over this area is greater than ~0.15. It will be called the high band depth area (HBDA) in the following. The second category is a wide area surrounding the first one with H_2O ice band depth not exceeding 0.15, which we call low band depth area (LBDA).

[31] H_2O ice band depth values are quite uniform over the HBDA, much more than CO_2 ice band depths. The polar erg departs from this uniformity with lower H_2O ice signatures. The evolution of the H_2O ice distribution in the HBDA is the same as the albedo distribution: it is axisymmetric from L_s 280° to L_s 50°, much less symmetric later on. H_2O frost is mostly confined to the permanent north polar cap at L_s ~90°. An increase of the H_2O ice band depth is observed over the HBDA throughout the recession.

[32] The LBDA stretches far to the south, down to 30°N. It very likely corresponds to detection of water ice in clouds. North polar water ice clouds are prevalent near the edge of the seasonal deposits in the spring and late summer/early fall, forming the polar hood [e.g., *Briggs and Leovy*, 1974; *James et al.*, 1994; *Leovy et al.*, 1972; *Christensen and Zurek*, 1984]. Polar hood clouds generally appear at L_s 160° [*Wang and Ingersoll*, 2002; *Kieffer and Titus*, 2001] and ~95% of the surface between 60°N and 75°N is shrouded in a cloud cover by L_s 185° [*Wang and Ingersoll*, 2002]. This polar hood persists during winter and retreats with the seasonal deposits during spring [*Wang and Ingersoll*, 2002], water ice clouds occurring within several degrees off the seasonal deposits edge [*James and Cantor*, 2001; *Tamppari et al.*, 2008; *Christensen and Zurek*, 1984;

Cantor et al., 2010]. We made a color composite image from the OMEGA visible channel to highlight these water ice clouds at L_s 35° (Figure 11). We chose the spectel at 699.7 nm for the red channel, at 535.9 nm for the green channel and at 476.0 nm for the blue channel. Scattering by water ice crystals is higher in the blue wavelengths than in the red ones, water ice clouds will thus appear bluish on a RGB mosaic [*James*, 1985; *Cantor et al.*, 2001; *Wang and Ingersoll*, 2002]. Water ice clouds are pointed by arrows on Figure 11a. There is a clear correlation between their location and the spatial distribution of the LBDA. Another discrimination criterium is provided by the 3 μm H_2O ice absorption band shape. A visual inspection of spectra acquired in the LBDA shows that this band has a sharply rising edge between 3.4 μm and 3.525 μm, characteristic of micron-scale H_2O ice particles in clouds [*Langevin et al.*, 2007]. Most of the LBDA thus corresponds to water ice clouds rather than surface water frost, while it is not excluded that part of the 1.5 μm absorption is due to surface frost on the north edge of the LBDA. This wide low band depths area is no more observed after L_s 70° which is consistent with TES observation of the progressive north polar hood breakdown at L_s ~75° [*Tamppari et al.*, 2008].

3.2. Boundaries of the Deposits

[33] The boundaries of the deposits in term of albedo, CO_2 ice and H_2O ice were retrieved from the OMEGA data set. They are compared to MOC and TES albedo boundaries and to TES and THEMIS infrared boundaries. Figures 12 and 13 illustrate the process followed to retrieve these boundaries. Figures 12 and 13 correspond to two different types of spatial evolution of the H_2O ice band depth.

3.2.1. Albedo Boundary

[34] The MOC camera achieved the most complete set of observations of the northern seasonal deposits. The bound-
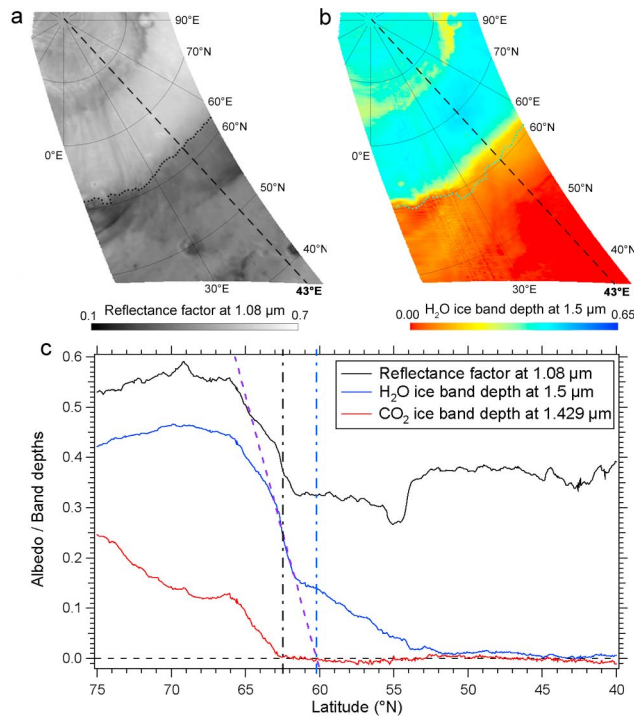
Figure 12. (a) Reflectance factor at 1.08 μm for OMEGA observation 2742_1 (L_s 18.7°). (b) The 1.5 μm H_2O ice band depth for the same observation. (c) Evolution of the reflectance factor at 1.08 μm (black curve), 1.429 μm CO_2 ice band depth (red curve) and 1.5 μm H_2O ice band depth (blue curve) as a function of latitude along longitude 43°E (black dashed line on Figures 12a and 12b) for this observation. The purple dashed line is the fit of the sharp decrease in the H_2O ice band depth profile (see text). The dash-dotted black line at 62.5°N corresponds to the albedo boundary of the seasonal deposits while the dash-dotted blue line at 60.2°N corresponds to the H_2O ice boundary. These boundaries are plotted as dotted curves on Figures 12a and 12b.

ary of the seasonal ices was monitored thanks to their high albedo on MOC data. These boundaries were hand drawn for each mosaic, the deposits outer limit being located by visual inspection of the spatial albedo variation [*Benson and James*, 2005]. The same work was done on MARCI data covering spring 29 [*Cantor et al.*, 2010]. We mostly used the same technique to retrieve the albedo boundary on OMEGA observations. Isoalbedo contours were drawn on each observation. The contour fitting the best the albedo edge of the deposits was chosen by visual inspection. For example, the albedo boundary is located at 43.0°E/62.5°N on Figure 12a and at 19.0°E/65.0°N on Figure 13a. As we can notice it does not correspond to the end of the albedo decrease on Figures 12c and 13c. Nevertheless, we used this method so as to make reliable comparisons with spring retreats monitored by MOC and MARCI. A low contrast between ices and defrosted soil can make the boundary more difficult to distinguish. In these situations, we used color composite mosaics from the OMEGA visible channel to enhance the contrast between frost and defrosted soil. As visible wavelengths are more sensitive to aerosol scattering than IR wavelengths, the presence of clouds along the edge

of the deposits can also cause confusion. We estimate the uncertainty on the albedo boundary latitude to be m 0.5°.

[35] No albedo boundary can be identified from L_s 280° to L_s 340° as the albedo of the seasonal deposits is then similar to that of outlying ice-free areas. The boundary is determined between L_s 350° and L_s 67°. After L_s 67°, the spatial coverage of OMEGA is too small to retrieve a reliable boundary. OMEGA, MOC, and MARCI albedo boundaries were zonally averaged for each mosaic and plotted on the same graph (Figure 14). There is a very good agreement between MOC and OMEGA MY 28 albedo boundaries, slight discrepancies being within error bars. A general agreement is observed between the five boundaries, indicating that the retreat is very similar between different Martian years. A plateau in the north polar regression curve during early to midspring has been reported by ground-based observers [*Capen and Capen*, 1970; *Iwasaki et al.*, 1979, 1982, 1999] and has been also observed by the Viking orbiters [*James*, 1979]. During this anomaly, the boundary of the seasonal deposits remains at a fixed latitude of about 65°N for several weeks before the retreat resumes. However, such a plateau is not observed on OMEGA, MOC and MARCI regression curves. The only major difference between these five boundaries is that the MOC boundary of MY 26 is shifted southward the other boundaries. This shift is up to 2°. Northern plains were thus covered by seasonal frost for a longer time during MY 26.

[36] The latitudinal evolution of this limit as a function of Martian days has been estimated. We obtain a mean recession speed of 0.11° of latitude (~6.2 km) per Martian day
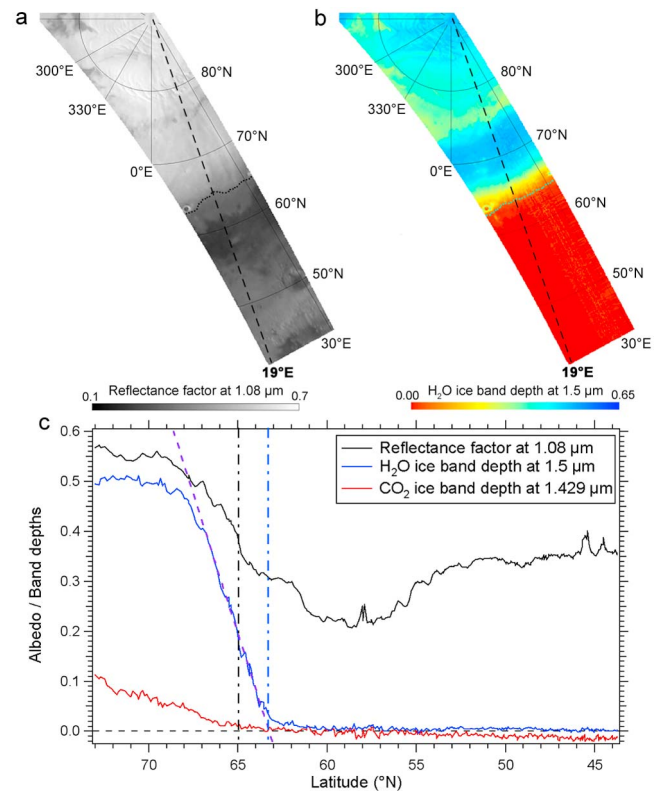
Figure 13. Same as Figure 12 but for OMEGA observation 2879_1 (L_s 36.4°).
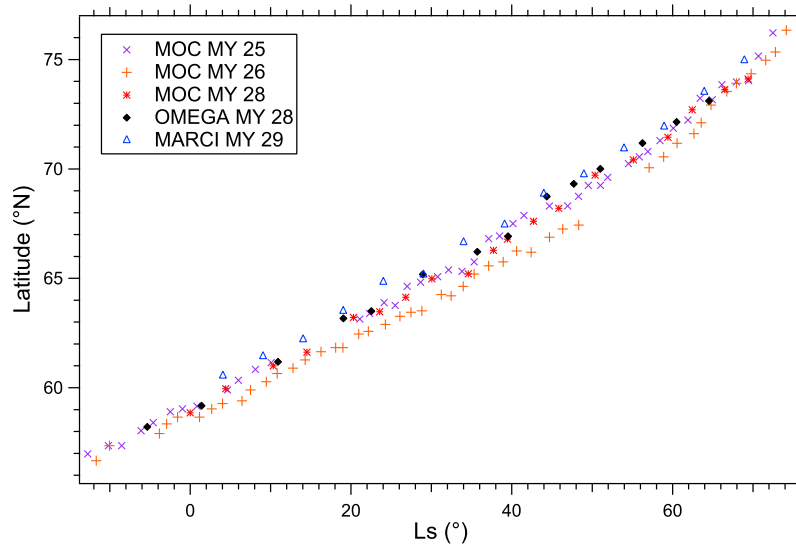
Figure 14. Retreat of the northern seasonal deposits as observed by MOC during MY 25 (purple crosses), MY 26 (orange pluses) and MY 28 (red stars), by OMEGA during MY 28 (black diamonds) and by MARCI during MY 29 (blue triangles). The latitude of the zonally averaged albedo boundaries is plotted versus aerocentric solar longitude.

which is consistent with observations performed during previous Martian years [*James and Cantor*, 2001; *Benson and James*, 2005; *Kieffer and Titus*, 2001; *Cantor et al.*, 2010].

3.2.2. CO₂ Boundary

[37] The formula giving the CO_2 ice band depth (see section 2.2.2) is adjusted so that the global average band depth value for regions surrounding the CO_2 deposits is equal to 0. But this zero level can fluctuate from one observation to another by ±0.02. In order to determine locally the latitude at which the CO_2 ice has disappeared, we evaluate the local mean value of the CO_2 ice band depth zero level for each observation. Then the boundary is defined as a threshold of 0.015 above this local mean zero level. For example, the CO_2 boundary is located at 43.0°E/ 63.0°N on Figure 12c and at 19°E/67.0°N on Figure 13c. We estimate the uncertainty on the CO_2 ice boundary to be ±0.3° in latitude. No CO_2 ice boundary is drawn after L_s 49° since the CO_2 ice distribution becomes patchy. The CO_2 ice boundary is plotted as a black line on CO_2 ice maps (Figures 4–7). It can be compared with the TES "crocus line" (see section 3.2.4).

3.2.3. H₂O Boundary

[38] The latitudinal profile of H_2O ice band depth on Figure 12c presents a two-step decrease. The first decrease is sharp, and the second is more gradual. These two decreases correspond to the two areas with H_2O ice described in section 2.2.3. We clearly see these two regions on Figure 12b. The gradual decrease likely corresponds to absorption by water ice in clouds. Therefore the H_2O frost boundary does not correspond to the end of the H_2O ice band depth gradual decrease on Figure 12c. However, on Figure 13c, there is only a one-step almost linear sharp decrease. In that case, the H_2O frost boundary corresponds to the end of the sharp decrease, at ~63°N. We assume that the H_2O ice band depth would decrease sharply and linearly until reaching the 0 level on Figure 12c if there was no absorption by water ice in clouds.

Therefore we fitted by a straight line the sharp decrease of the H_2O ice band depth in both cases (purple line) and determined the intersection point between this line and the 0 band depth level. This technique works for a one-step sharp decrease and for a two-step decrease as well. On Figure 12, the H_2O ice boundary is then located at 60.2°N. On Figure 13, it is located at 63.3°N. We estimate the error on the H_2O ice boundary at ~0.5° in latitude. No H_2O ice boundary is drawn after L_s 67° since the spatial coverage of OMEGA is too limited for a reliable analysis. The H_2O ice boundary is plotted as a blue line on CO_2 ice maps (Figures 4–8).

3.2.4. TES Crocus Line

[39] The last type of boundary we study is the TES crocus line. The crocus line is a thermal boundary corresponding to latitudes and longitudes where the 30 μm brightness temperature rises above 165 K for a given L_s [*Kieffer and Titus*, 2001]. The threshold temperature is set slightly higher than the CO_2 ice temperature (~150 K) to account for the mix of surface temperatures that occurs in a latitude strip in spring [*Kieffer and Titus*, 2001]. TES was operating in a degraded mode at the end of the MGS mission, in 2006. Therefore bolometer temperatures where used instead of 30 μm brightness temperatures to draw the MY 27–28 TES crocus line. Bolometer temperatures are more sensitive to the atmospheric temperature, resulting in a crocus line shifted northward the three previous crocus lines (T. Titus, personal communication, 2009). We decided to use the average of these three previous crocus lines, i.e., MYs 24–25, 25–26, and 26–27, instead of the MY 27–28 crocus line. The mean latitudinal difference for a given longitude and L_s between these three crocus lines is 0.6°. This mean crocus line is plotted on each mosaic as a dashed line. The L_s value for which it is plotted corresponds to the mean of each L_s interval.

3.2.5. Asymmetry of the Retreat

[40] Even though the seasonal deposits seem axisymmetric at the beginning of their retreat, some longitudinal variations
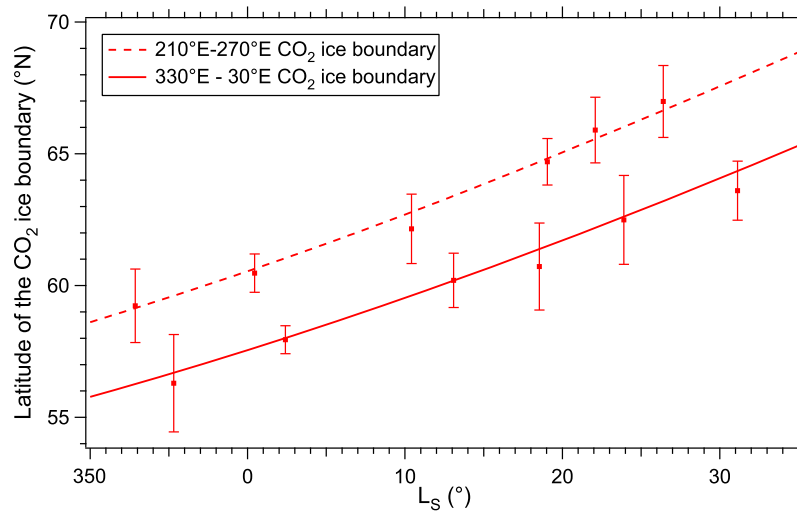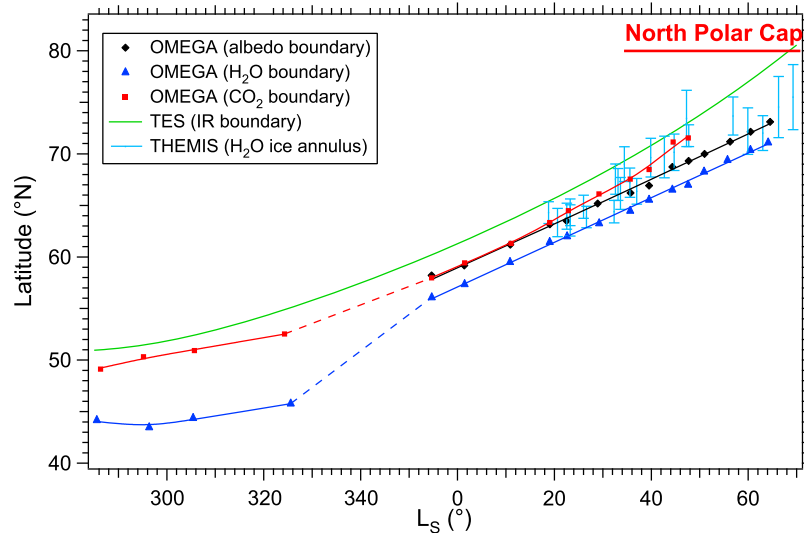
Figure 15. Spring evolution of the CO_2 ice boundary for longitudes 210°E to 270°E (dashed line) and 330°E to 30°E (solid line). The error bars refer to a latitude dispersion of $\pm 2\sigma$ within each longitude range.

exist. The longitude segment 330°E–30°E is the slowest to regress, while the 210°E–270°E segment regresses the quickest, whatever the kind of boundary (albedo, CO_2 or H_2O). This asymmetry is observed with MOC data during MY 24–25 and 25–26 for the same longitude segments [*James and Cantor*, 2001; *Benson and James*, 2005]. The CO_2 ice boundary recession curve is plotted for the longitude segments 330°E–30°E and 210°E–270°E in Figure 15. The temporal shift between the two curves is ~15° L_s, which corresponds to ~32 Martian days. The spatial shift is about 3.2° of latitude. A Mars Orbiter Laser Altimeter (MOLA) map of the north polar region shows that the 330°E–30°E segment corresponds to the lowest elevations of the circumpolar region, while the 210°E–270°E is slightly above average in elevation [*Zuber et al.*, 1998]. The higher pressure in the lower regions entails a higher radiative equilibrium temperature for the CO_2 ice [*Fray and Schmitt*, 2009], and thus a higher emitted thermal flux. It is compensated during winter by a higher condensation flux. Therefore the asymmetry observed is consistent with an enhancement of CO_2 condensation in the lower regions and thus a larger initial CO_2 ice depth. The condensation in the 210°E–270°E segment could also be influenced by strong weather patterns, such as an enhancement of the energy advection by the active storm zone in this longitude range [*Hollingsworth et al.*, 1995]. But other parameters such as the albedo of the ice during its sublimation phase could also be involved in this asymmetry, as it has been observed for the southern seasonal deposits recession [*Schmidt et al.*, 2009]. A statistical analysis of the parameters involved in the thermal equilibrium controlling the condensation and sublimation of the ice needs to be performed to clearly understand the origin of this asymmetry.

3.2.6. Intercomparison Between the Boundaries

[41] All these limits are zonally averaged and plotted on the same graph (Figure 16). First we observe that the H_2O ice boundary is systematically shifted south of the CO_2 ice boundary. It implies that a CO_2-free water ice annulus surrounds the receding CO_2-rich deposits. This water ice annulus corresponds to the one detected by TES and THEMIS on the basis of temperature measurements [*Kieffer and Titus*, 2001; *Wagstaff et al.*, 2008]. We notice that this water ice annulus is very extended, down to 43°N and ~6° wide, before the beginning of its recession at L_s 330°. This wide winter H_2O ice annulus likely corresponds to the thin water ice frost observed to vary daily by the Viking Lander 2 at 48°N in Utopia Planitia [*Jones et al.*, 1979; *Hart and Jakosky*, 1986; *Svitek and Murray*, 1990], i.e., condensation of water ice during the night and partial sublimation during the day. After L_s 350°, the water ice annulus is only 2.0 ± 0.8° wide. Then the CO_2 ice boundary gradually recesses between L_s 20° and 50° thus widening the annulus to ~4.6° by L_s 50°. After this date, it is hard to define an annulus since the CO_2 ice distribution becomes patchy but at that time CO_2-free H_2O ice areas begin to appear at all latitudes. The extension of the water ice annulus determined by OMEGA is thus clearly smaller than the ~5° extension measured by TES during the MY 24–25 recession [*Kieffer and Titus*, 2001]. *Wagstaff et al.* [2008] report on the location and extent of the water ice annulus on the basis of THEMIS temperature measurements. These observations are plotted as light blue vertical bars on Figure 16. The extension and location of the water ice annulus detected by THEMIS are in good agreement with OMEGA observations between L_s 20° and 40° except for occasional THEMIS detections shifted north compared to OMEGA detections at L_s ~35°. Then, between L_s 40° and 50°, THEMIS detections are systematically shifted more than 2° north OMEGA detections but the annulus extension still agrees. Discrepancies on the annulus location may come from the inhomogeneous coverage of THEMIS: THEMIS values correspond to observations made at specific longitudes while OMEGA boundaries are averaged over all longitudes. After L_s 60°, the southern boundary of the THEMIS water ice annulus corresponds to the OMEGA H_2O ice boundary. The evolution of the water ice annulus extent is therefore mostly similar on OMEGA and

Figure 16. Winter and spring evolution of the albedo (black diamonds), H_2O ice (blue triangles) and CO_2 ice boundaries (red squares) observed by OMEGA are compared to TES crocus line (green curve) and water ice annulus extent observed by THEMIS (light blue curve). All limits have been zonally averaged. No CO_2 ice limit is plotted after L_s ~50° since the CO_2 ice band depth distribution is too patchy to define a reliable CO_2 boundary. CO_2 and H_2O ice boundary evolution is plotted with dashed lines between L_s 325° and 355° because of the lack of data for this range of L_s. The averaged latitude of the north polar cap boundary is 80°N (horizontal red line).

THEMIS observations, but the annulus location diverges between the two instruments, maybe due to differences in spatial coverage.

[42] One can also notice that the albedo limit of the seasonal deposits does not correspond to their outer limit, i.e., the water ice limit. A shift of ~2° of latitude is observed between these two limits. However, we see on Figure 13c that albedo and H_2O ice band depth stop decreasing at about the same latitude, ~63°N. The origin of this shift is thus just due to the different methods used for determining the albedo "limit" (about midway of the decrease of the albedo contrast between ices and defrosted soil, determined by visual inspection) and the water ice limit (total disappearance of the ice signature). The "albedo boundary" given by this method tends to be located slightly northern than the true end of the albedo decrease. Water ice detected by OMEGA south of the visually located albedo limit has a lack of visual contrast with the bare defrosted soil and thus cannot be detected in the visible range, at least at the OMEGA spatial resolution. This water ice is probably dusty and spatially segregated at subpixel scale with already defrosted soil. Such a patchy configuration has already been observed by MOC [see *Malin and Edgett*, 2001, Figure 44b] and by the HiRISE camera onboard MRO, at a higher spatial resolution (Figure 17).

[43] Albedo and CO_2 ice boundaries of the seasonal deposits are first similar but after L_s 20°, the CO_2 ice boundary regularly shifts north of the albedo boundary. It implies that the water ice annulus is only made of dusty water ice spatially segregated with defrosted soil before L_s 20°. Then the annulus is made of both a constant ~2° wide southern dusty and patchy water ice area and a northern brighter area with an extension which gradually increases to ~2° at L_s 50°.

[44] One can also observe that our CO_2 ice boundary is systematically shifted ~2° south of the TES crocus line. However, these two boundaries do not correspond to the same spatial amount of CO_2 ice covering the surface. The surface temperature threshold for the TES crocus line is set to 165 K, i.e., 15 K above the CO_2 ice temperature, to account for the spatial mix of surface temperatures occurring during spring. A quick calculation indicates this surface temperature is obtained with a surface covered by 81% of CO_2 ice at 150 K and only 19% of H_2O ice at 205 K. We set the CO_2 ice temperature to 150 K since it is its equilibrium temperature at 9 mbar [*Fray and Schmitt*, 2009], the mean surface pressure measured by Viking Lander 2 between L_s 0° and 70° [*Hess et al.*, 1980]. The same temperature was measured by TES over the CO_2-rich ice during MY 24–25 northern winter and spring [*Kieffer and Titus*, 2001]. The H_2O ice temperature is set to 205 K since it is its equilibrium temperature at 9 mbar [*Fray and Schmitt*, 2009], assuming a water vapor mixing ratio in the low atmosphere of 0.03% [*Owen*, 1982]. The TES crocus line does not correspond to the disappearance of CO_2 ice on the surface but to the rise of surface temperature due to segregation between CO_2 and H_2O ices. The OMEGA CO_2 ice boundary is defined as the end of this segregation with almost total disappearance of CO_2 ice on the surface.

3.3. Evolution of the Seasonal Deposits Stratigraphy

[45] An important issue is the growth of the bright northern part of the water ice annulus after L_s 20°. Visual inspection of the CO_2 maps indicates that this phenomenon is correlated with a faster decrease of the area covered by the CO_2 ice signature leading to its patchy distribution by L_s 50°. In particular, many disappearances of the CO_2 ice signature are observed in regions located north the TES crocus line,
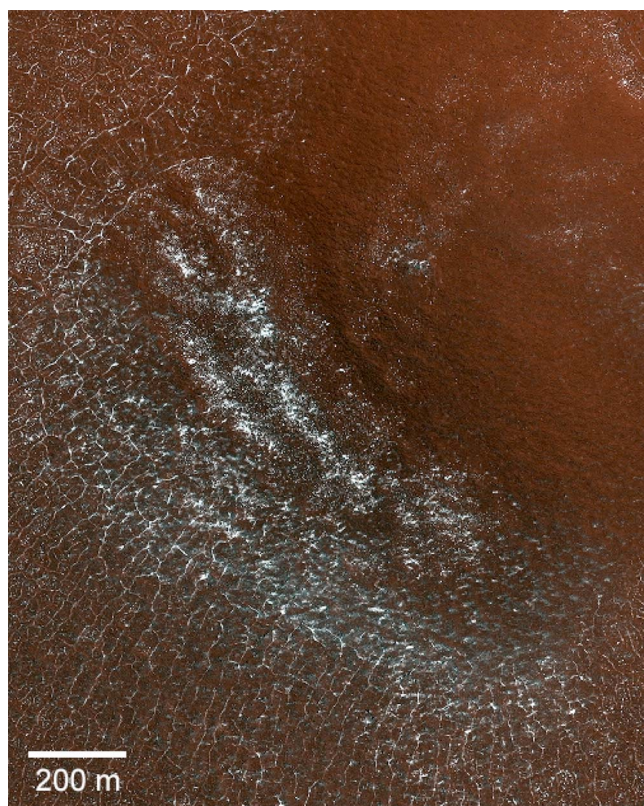
Figure 17. Segregation between frost and defrosted soil observed by the HiRISE camera (PSP_007642_2480, 67.8°N, 234.0°E, L_s = 44.7°).

such as Olympia Planitia and the top of Gemina Lingula (see Figure 8b). Surface temperature therefore indicates the presence of abundant CO_2 ice in these regions but its spectral signature is absent. We thus conclude that CO_2 ice is overlaid by an optically thick cover, either of dust or of water ice, the two minor components included in CO_2-rich ice.

[46] Adding an optically thick layer of dust on CO_2-rich ice would strongly decrease the observed albedo, which is not the case as it remains the same or even increases south of the CO_2 ice boundary. A water ice frost layer overlying CO_2 ice is consistent with the observations of both high albedos and H_2O ice signatures in regions where the CO_2 ice signature disappears. The following scenario can be proposed for the formation of this optically thick water frost layer: at the beginning of northern spring, a thick layer of CO_2 ice contaminated by H_2O ice and dust particles covers the northern regions. We extracted a typical spectrum of this ice and modeled it so as to estimate the proportion of each component and its grain size (Figure 18). The OMEGA spectrum is extracted at 65.3°N/341°E from observation 2621_1 acquired at L_s = 2.4°. It has been corrected for atmospheric absorption by a radiative transfer code developed by *Douté* [2009]. No aerosol correction has been made so the reflectance factor in the continuum and CO_2 and H_2O ices band depths may be reduced by 10 to 30% from their expected value for a "clear atmosphere" [*Vincendon et al.*, 2007]. Using a radiative transfer model in layered media [*Douté and Schmitt*, 1998] and optical constants of CO_2 and

H_2O ices [*Quirico and Schmitt*, 1997; *Grundy and Schmitt*, 1998; *Schmitt et al.*, 1998], we model this spectrum by an intimate mixture of 7 cm CO_2 ice grains contaminated by 0.19 wt % of 200 μm H_2O ice grains and 0.06 wt % of 13 μm dust particles with uncertainties of the order of 20% coming from the lack of aerosol correction. The model fits well for the 1–2.5 μm spectral range while strong discrepancies are observed for wavelengths greater than 2.5 μm. It may be due to the early presence of a very thin layer of H_2O ice above the CO_2-rich ice. The exact composition of this water ice layer is beyond the scope of this paper and will be determined elsewhere. The aim here was to estimate the bulk composition of the CO_2-rich deposit. Soon after spring sunrise, the incident solar flux is large enough to sublimate CO_2 ice but not the H_2O ice grains trapped in it. A fine grained H_2O ice layer gradually forms by segregation of the ice grains embedded in the CO_2 ice and it is left at the surface as the CO_2 ice sublimes. This layer of H_2O grains progressively builds up and it eventually becomes optically thick, hiding the spectral signature of the underlying CO_2-rich ice. Radiative transfer modeling shows that a 200 μm thick layer of H_2O ice is sufficient to completely hide the CO_2 ice band at 1.43 μm (Figure 19). We modeled the CO_2-rich ice by the intimate mixture we previously determined (see Figure 18) and the layer of H_2O ice above this CO_2-rich ice by 200 μm H_2O ice grains. We found that a H_2O layer with a thickness similar to the grain size is already able to completely hide the 1.43 μm CO_2 ice band as well as the other CO_2 ice bands between 1 and 4 μm.

[47] *Cull et al.* [2010] analyzed Compact Reconnaissance Imaging Spectrometer for Mars (CRISM) spectra acquired during spring over the Phoenix landing site and observed the early disappearance of the CO_2 ice spectral signature. They propose an alternative interpretation for this early disappearance: as CO_2 ice sublimes, it disintegrates into smaller grains which reduces its spectral signature. They model CRISM spectra by a layer of soil overlaid by an intimate mixture of CO_2 ice, H_2O ice and dust of decreasing thickness, amount and grain size of CO_2 ice. An analysis of their modelizations led us to conclude that their interpretation is not correct. First of all, their modelizations do not fit correctly CRISM spectra at wavelengths where CO_2 ice absorbs. The CO_2 ice signature decreases in CRISM spectra and is no more observed by L_s 20° while modelizations of *Cull et al.* [2010] clearly show the 1.43 μm CO_2 ice absorption band at L_s 20° and 26° with no obvious band depth decrease [see *Cull et al.*, 2010, Figure 7]. Furthermore, for large grain sizes decreasing the grain size of CO_2 ice while keeping its amount constant in an intimate mixture results in an increase of the continuum reflectance and thus in an increase rather than a decrease of the 1.43 μm CO_2 ice band depth. This situation is illustrated by radiative transfer modeling we made in an ice layer of the same composition than that of *Cull et al.* [2010] (see Figure 21). We also modeled the decrease of the CO_2-rich layer thickness while keeping constant the amount of CO_2 ice and its grain size. It results in a decrease of the reflectance factor in the continuum but not in the medium to strong absorption bands; the CO_2 ice band depth (relative to continuum) therefore decreases but does not disappear. By decreasing the CO_2 ice amount with a constant grain size and layer thickness and increasing correspondingly the amount of H_2O ice, the CO_2 ice signature
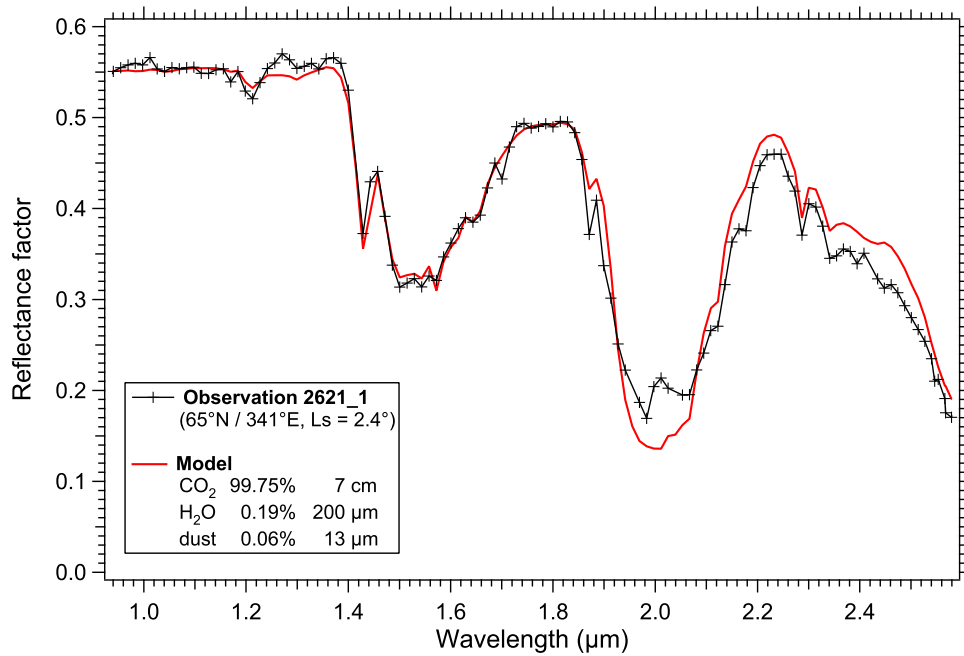
Figure 18. Modeling of a typical spectrum of the CO_2-rich ice deposits in the early stage of the retreat ($L_s = 2.4°$). Black line with crosses is observed spectrum of seasonal deposits. Red line is modeled spectrum assuming a granular mixture of CO_2 ice with inclusions of H_2O ice and dust. Components percentages are weight percentages.

also decreases without disappearing and H_2O ice absorption increases. Therefore a simple evolution of CO_2 ice amount and/or grain size in the layer is not enough to explain the early disappearance of the CO_2 ice signature. It requires the build up of an optically thick layer of H_2O ice.

[48] This scenario of evolution also explains the increase of the water ice annulus extent after L_s 20°. It is known from GRS and MOLA observations that the thickness of the seasonal deposits increases from the outer condensation limit at ~50°N to the pole where the thickness is of the order of
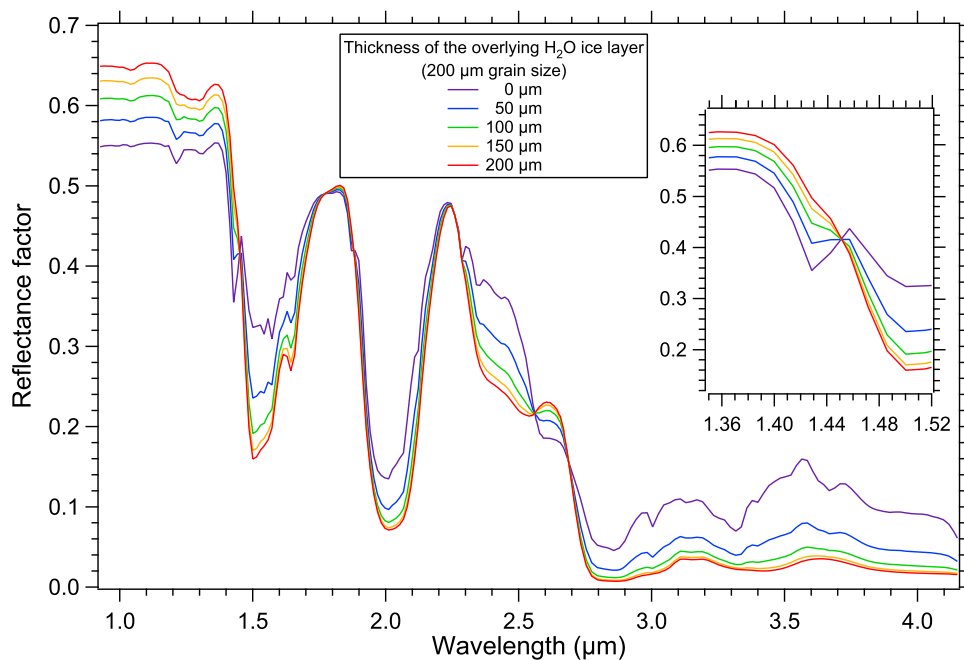
Figure 19. Modeled spectra of CO_2 ice containing H_2O ice and dust particles and overlaid by a layer of 200 μm grain size H_2O ice with various thickness. Notice that a H_2O ice layer with a thickness lower than the H_2O ice grain size corresponds to a partial coverage of the CO_2-rich ice by H_2O ice.
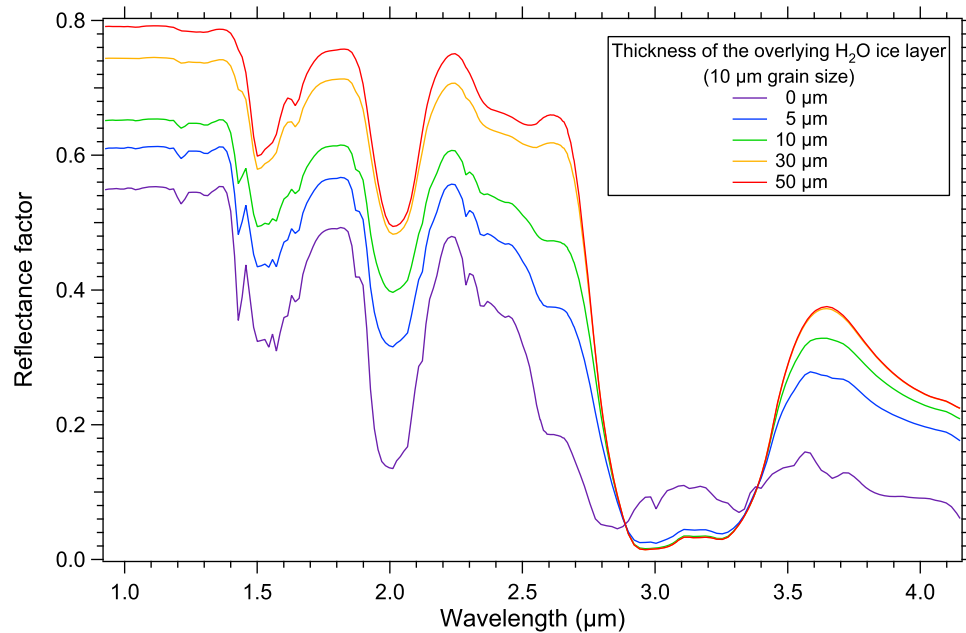
Figure 20. Modeled spectra of CO_2 ice containing H_2O ice and dust particles and overlaid by a layer of 10 μm grain size H_2O ice with various thickness.

1 m [*Smith et al.*, 2001; *Mitrofanov et al.*, 2003; *Aharonson et al.*, 2004]. If we assume that the fractional abundance of H_2O ice in the seasonal deposits before their retreat is mostly constant with latitude, then a column of seasonal deposits located at higher latitude will contain more H_2O ice. Therefore, the total amount of H_2O ice grains released at the surface by the sublimation of CO_2-rich ice along the border of the CO_2 deposits increases with latitude, and thus L_s. The southernmost sublimating CO_2-rich deposits will thus be progressively hidden by an overlying layer of released H_2O ice grains, with increasing thickness with latitude. This surficial optically thick layer leads to an apparent increase of the water ice extent at higher latitudes. The growing northern part of this water ice annulus has a higher albedo since it consists of sublimating CO_2-rich ice overlaid by optically thick H_2O ice instead of H_2O ice spatially segregated with defrosted soil for the southern regions.

[49] Cold trapping of water vapor coming from the sublimating part of the water ice annulus may also explain the growing of its bright northern part and the early disappearance of the CO_2 ice signature at higher latitudes. The amount of water ice contained in the water ice annulus should increase with latitude, or L_s, since it is composed of water ice from the CO_2-rich ice added to the early H_2O frost deposited over the soil during fall, with thickness probably also increasing with latitude. Thus an increasing amount, and flux, of water vapor is released to the atmosphere by the sublimation of the water ice annulus. Due to baroclinic wave activity at the edge of the deposits, part of this water vapor can diffuse northward over the CO_2-rich ice and be either cold trapped directly at the surface of the CO_2-rich ice or condense in the cold near-surface atmospheric layer and settle on the surface, as suggested by *Houben et al.* [1997]. The exact size of H_2O ice grains condensed by cold trapping of water vapor on CO_2-rich ice is not known. The mechanism of cold trapping of water vapor is invoked

by *Bass et al.* [2000] to explain the late summer brightening of the north permanent cap. This brightening is well reproduced by an ice deposit 10 to 50 μm thick. Furthermore, it is consistent with the *Hart and Jakosky* [1986] estimates of approximately 10 μm of ice deposited at the Viking Lander 2 site. Therefore we consider that water vapor should condense on CO_2-rich ice in the form of H_2O ice grains about, or less than, 10 μm in size. Radiative transfer modeling shows that a 60 μm thick layer of 10 μm grain H_2O ice is sufficient to completely hide the CO_2 ice band at 1.43 μm (Figure 20). The building of a water ice layer made of 10 μm grains results in a large increase of the albedo but a stable H_2O ice band depth. Successive increases of albedo (+50–60%) and then of H_2O ice band depth (+20–30%) are observed at locations where the CO_2 ice signature disappears. Therefore the layer of water ice hiding the CO_2 ice signature should be made of a mix of H_2O ice grains coming from the two sources: H_2O grains inside the CO_2 seasonal ice layer and water vapor trapped at its surface. The analysis of the exact composition and texture of this overlying water ice layer and of its temporal evolution, not in the scope of this paper, should give us clues on its origin(s) and evolution process(es) and will thus constrain the mobility of water vapor coming from the sublimating part of the water ice annulus and from subsequent desorption of soil minerals [*Beck et al.*, 2010] (Figure 21).

[50] We previously reported on the overall brightening of the northern seasonal deposits during their retreat (see section 3.1.1). Many mechanisms have been invoked to explain this brightening. The gradual building of an optically thick layer of H_2O ice over CO_2-rich ice certainly contributes to this brightening since radiative transfer modeling shows that this configuration leads to an increase of the albedo of typically 20–50% depending on the upper layer H_2O grain sizes (Figures 19 and 20).
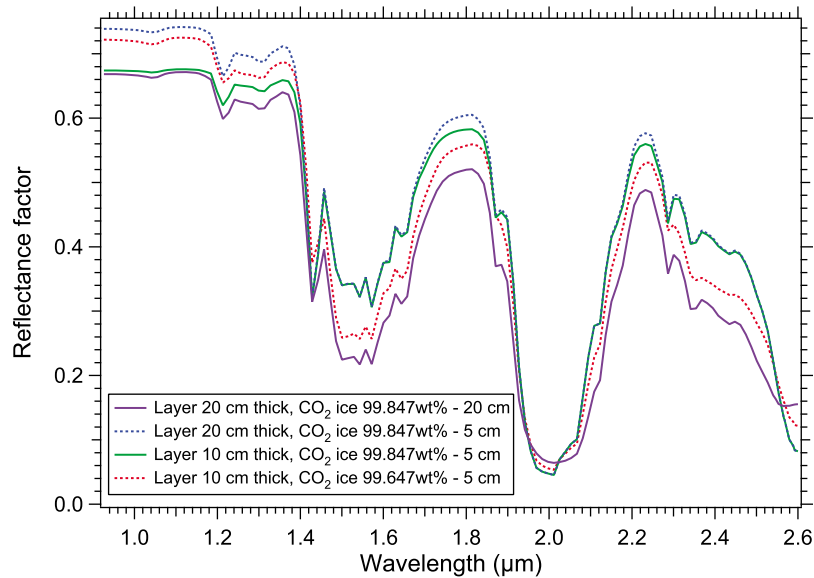
Figure 21. Modeled spectra of a layer of soil overlaid by an intimate mixture of CO_2 ice, H_2O ice and dust. Purple solid line is a 20 cm thick layer of 99.847 wt % CO_2 ice (20 cm grain size) + 0.15 wt % H_2O ice (200 μm grain size) + 0.003 wt % dust (13 μm grain size) overlying a layer of soil (30 μm grain size). Blue dashed line is same thickness and composition but with 5 cm CO_2 ice grains. Green solid line is same composition and grain size but the layer is 10 cm thick. Red dashed line is a 10 cm thick layer of 99.647 wt % CO_2 ice (5 cm grain size) + 0.35 wt % H_2O ice (200 μm grain size) + 0.003 wt % dust (13 μm grain size) overlying a layer of soil (30 μm grain size).

[51] Between L_s ~50° and 70°, the CO_2 ice signature strongly reappears in locations where it had previously disappeared. This behavior occurs mostly on the circumpolar dark dunes field and in spiral troughs over the north permanent cap (Figure 8c and 8d). We also observe strong increases of the CO_2 ice signature in locations where it had not completely disappeared. Since we observe the modification of the CO_2 ice band depth by comparing two successive maps with a time lag of less than 4° of L_s, these late increases are very sharp. In the following, the late increases of the CO_2 ice signature are called LICS events. We have demonstrated that the formation of a H_2O ice layer over the sublimating CO_2-rich ice is responsible for the early disappearance of the CO_2 ice signature. Thus LICS events may be due to either the removal of this H_2O ice layer or to condensation of CO_2 ice over this water ice layer. Erosion by katabatic winds over the northern cap and venting processes over the dark dune erg are most likely responsible for the disruption of the overlying H_2O ice layer and/or recondensation of CO_2 ice which leads to LICS events. These mechanisms require a specific discussion which is beyond the scope of this article and will be discussed in detail in a future article.

[52] Early disappearances of the CO_2 ice signature are not systematically followed by LICS events. For example, we observe the disappearance of the CO_2 ice signature at L_s ~60° on top of Gemina Lingula but no increase of the CO_2 ice signature later. In this location, the CO_2 ice remains hidden below the upper millimeters thick water ice layer until its complete sublimation. To summarize, the gradual building of a water ice layer overlying the CO_2-rich deposits after L_s 20° is the general behavior observed on the northern seasonal deposits. It results in the early disappearance of the CO_2 ice signature on many locations, followed locally by the late increase of the CO_2 ice signature. LICS events are also observed in locations where the overlying water ice layer was not thick enough to hide the CO_2 ice signature.

4. Discussion and Conclusion

[53] From the spatial and temporal evolution of albedo and ices band depths, we propose a scenario that describes the late winter and spring evolution of the northern seasonal deposits (Figure 22). Figure 22a corresponds to the state of the seasonal deposits soon after the beginning of the recession, at L_s ~320°. They are composed of two layers: a bottom layer of H_2O ice and an overlying layer of CO_2 ice contaminated by H_2O ice and dust. This layering is the result of the condensation stages that occurred during late autumn and winter. First the condensation of water frost starts during the night with water frost sublimating completely during the day. The latitude-time dependence of the first frosts will depend on the partial water vapor pressure in the atmosphere. In a second step, when the sun is low enough, the frost persists all day long [*Jones et al.*, 1979]. At this stage the accumulation rate should increase due to the positive feedback of the surface albedo on the thermal balance. This frost may also partly diffuse into the upper layer of soil and be adsorbed on mineral grains [*Beck et al.*, 2010] or possibly form some ice-cemented crust. Vapor diffusion and condensation at some depth will occur if there is a negative thermal gradient at some time of the daily cycle. In a second stage, when the thermal balance allows the surface temperature to drop below the CO_2 freezing point, CO_2 frost can start to condense including tiny amounts of water ice grains and
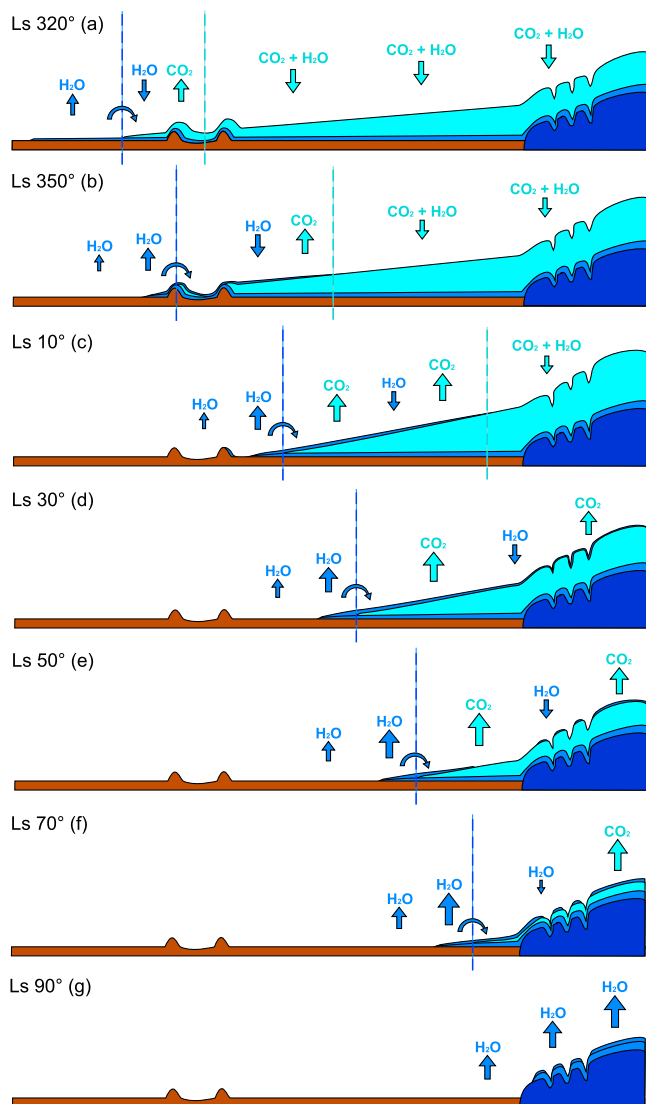
Figure 22. Possible sketch of the temporal evolution of the northern seasonal deposits. Latitudinal cross sections of the seasonal deposits show increasing L_s with vertical scale not respected for clarity. Dark blue is water ice in the north permanent cap (right). Medium blue is dusty water ice composing the underlying frost and the water ice annulus. Light blue is the CO_2-rich ice contaminated with dust and water ice. The dashed light blue line corresponds to the condensation/sublimation transition of CO_2 ice while the dashed medium blue line corresponds to the condensation/sublimation transition of H_2O ice. For clarity, water ice clouds and hazes are not represented. They are present within several degrees off the seasonal deposits edge until $L_s \sim 70°$. See text for complementary explanation.

dust particles (see Figure 18). This condensation should be first a diurnal condensation/sublimation cycle but at high latitudes, typically north of a latitude 5°–10° below the midday terminator, condensation will occur continuously at a rate mostly determined by the surface CO_2 thermal emission and subsurface conduction [*Forget et al.*, 1999;

Lewis et al., 1999]. At lower latitudes, where the daily average thermal balance is negative and net accumulation occurs, the condensation/sublimation diurnal cycle should still be effective. The thin water frost underneath should then be "frozen" at the CO_2 ice temperature and water vapor diffusion inside the regolith is no longer efficient. The initial H_2O frost condensation and its associated surface albedo increase should help in lowering the surface temperature and thus may initiate CO_2 condensation earlier, or at lower latitude, than without this precursor frost. The result should be a layer of CO_2-rich ice with a thickness gradient from the outer condensation limit at about 50° latitude to the pole, with a thickness of the order of 1 m [*Smith et al.*, 2001; *Mitrofanov et al.*, 2003; *Aharonson et al.*, 2004] on top of a millimeters thick layer of H_2O frost and of centimeters of icy soil. To what extent microphysical evolutions of these frosted soil, H_2O frost and CO_2 ice layers may occur during these condensation stages is still an open question. A striking example is the observation of transparent frost in northern winter, at L_s 329° (Figure 10). It suggests that CO_2-rich deposits could be initially in slab form. Based on physical models, seasonal CO_2 deposits on Mars can undergo seasonal densification into a nonporous, polycrystalline layer, provided freshly condensed grains are sufficiently small (<10 μm) [*Eluszkiewicz*, 1993]. CO_2 slab ice has been invoked to explain the observations of cold surfaces with low albedo in the so-called southern "cryptic" region [*Kieffer et al.*, 2000], interpreted either as translucent ice with partial dust contamination at the surface of the ice [*Kieffer*, 2007] or by extensive dust contamination close to the surface of a CO_2 ice layer [*Langevin et al.*, 2006]. This configuration is also observed near the edge of the northern seasonal deposits in winter. However, we have shown that CO_2-rich ice is no longer transparent at L_s 350°, so a change in the optical properties of the CO_2 frost has occurred between L_s 329° and L_s 350°. As CO_2 ice sublimes, the surface layer may disintegrate into smaller grains [*Titus et al.*, 2001] and lead to a nontranslucent CO_2 ice with an albedo higher than defrosted soil, if the contamination of CO_2 ice layer by dust is low enough, which is evidenced by spectral modeling (Figure 18). An alternative solution is that CO_2 ice stays in slab form as it sublimates, but a layer of fine grained H_2O ice forms on top of the sublimating CO_2 ice. As shown with spectral modeling (Figures 19 and 20), the formation of such a water frost layer results in a strong albedo increase. A more detailed spectral model is needed to specify which evolution scenario is actually occurring on Mars.

[54] CO_2-free water ice located on the left part of Figure 22a corresponds to daily water frost and initially extends about 6° latitude south of the observed edge of the CO_2-rich deposits. Progressive heating of the ice by the sun causes the CO_2 ice sublimation. Sublimation flux decreases with increasing latitude and condensation of CO_2 ice still occurs at high latitudes (Figure 22a). Transition between net condensation and sublimation of CO_2 ice is illustrated by a dashed blue vertical line. Since the H_2O ice radiative equilibrium temperature is higher than that of CO_2 ice, H_2O ice sublimation occurs at lower latitudes, unless partial water vapor pressure is above its saturation point, and condensation occurs over the cold CO_2 ice. A dashed medium blue line

illustrates the transition between condensation and sublimation of H_2O ice.

[55] Extension of ground covered by seasonal water frost decreases from L_s 320° to 350° since less water frost condenses during the night than sublimates during the day (negative net daily condensation balance). It leads to a narrow water ice annulus about 2° of latitude wide (Figure 22b). It is composed of the initial icy soil and of two H_2O ice layers: a bottom water frost layer condensed during late autumn and a top layer made of H_2O ice released by the sublimation of the CO_2-rich ice layer. H_2O ice previously contained in CO_2-rich ice also forms a thin layer overlying sublimating CO_2-rich ice located at higher latitudes. Water vapor is released by the sublimation of the water ice annulus (right upward "H_2O" arrow) and by water desorption and possibly dehydration from regolith minerals (left upward "H_2O" arrow) [Pommerol et al., 2009; Beck et al., 2010]. Part of this water vapor may diffuse in the low atmosphere toward higher latitude and be cold trapped on the CO_2-rich ice as suggested by Houben et al. [1997] and discussed by Bass and Paige [2000], and thus be added to the overlying water ice layer.

[56] Marked slope variations, as in craters, lead to spatial segregation between CO_2 ice and H_2O ice (Figure 22b). CO_2 ice on south facing slopes sublimates quicker than CO_2 ice on north facing slopes. It leads to north facing slopes covered by CO_2-rich ice and south facing slopes only covered by dusty H_2O ice. After complete disappearance of CO_2 ice, sublimation of water ice leads to north facing slopes covered by dusty water ice and defrosted south facing slopes (Figure 22c). This kind of spatial segregation is expected to occur at various scales: regional with regional topography; medium scale associated with features such as with craters and dunes; and low spatial scales associated with features like polygonal terrains.

[57] CO_2 ice condensation no longer occurs after L_s 30° (Figure 22d), and CO_2 ice sublimation flux increases with increasing solar flux. Accumulation of water ice previously contained in CO_2-rich ice thickens the overlying water ice layer. It results in the progressive hiding of the CO_2 ice signature on the border of the seasonal deposits and the gradual increase of the water ice annulus extent. It is important to note that we define this water ice annulus as the contiguous region located south of the CO_2 ice signature boundary in which the H_2O ice signature is spectrally detected. But regions located south of the CO_2 ice signature boundary may still be covered by CO_2 ice after L_s 20° since CO_2 may be hidden by an overlying optically thick layer of water ice. After L_s 20°, the water ice annulus is thus composed of a southern annulus made of a layer of dusty water ice and of a northern annulus with optically thick water ice overlying sublimating CO_2-rich ice. Temperature measurements at high spatial resolution may help to determine the exact extent of CO_2-rich ice on the ground. After L_s ~50°, the gradual build up of the water ice layer overlying sublimating CO_2-rich ice results in the disappearance of the CO_2 ice signature at many locations at high latitudes up to the north pole, thus destroying the annulus structure of the area displaying only water ice signature and resulting in a patchy distribution of the CO_2 ice signature. Then the H_2O ice overlying layer is disrupted locally (Figure 22e), and the CO_2 ice band depth suddenly increases. This late CO_2 ice signature increase preferentially

occurs on the circumpolar dark dunes field and in the numerous north permanent cap spiral troughs. It is observed until L_s 70° (Figure 22f). The overlying water ice layer is likely removed by katabatic winds in the spiral troughs and by venting process on the polar erg where there is also probably condensation of CO_2 ice above. At places where none of these processes occur, such as on the cap plateaus, the CO_2 ice remains hidden below the upper millimeters thick water ice layer but continue to sublimate until exhaustion. After L_s 70°, no new late increase of CO_2 ice signature occurs and the CO_2 ice band depth decreases at all places where the H_2O layer has been removed, until complete disappearance of CO_2 ice at L_s 80°.

[58] The final stage of the evolution of the seasonal deposits is the sublimation of the remaining dusty H_2O ice layer made of three different water ice sources: H_2O frost condensed on the ground during autumn, H_2O ice grains included in the CO_2 ice layer during its winter condensation, and H_2O vapor cold trapped over the CO_2 ice layer during the spring retreat. It corresponds to the large pulse of water vapor released in the atmosphere observed by Mars Atmospheric Water Detector (MAWD) and Infrared Thermal Mapper (IRTM) [Bass and Paige, 2000]. An open question is whether the annual water frost budget is positive or negative on the permanent north polar cap. If it is positive, water frost accumulates from year to year. On the contrary, a negative water frost budget means that the north permanent cap is losing mass from year to year.

[59] Northern seasonal deposits differ from the southern ones by the amount of H_2O ice involved. In the south the low amount of water trapped in the CO_2 ice [Langevin et al., 2007] precludes the formation of a water ice annulus and of an optically thick water ice layer on top of the CO_2 ice. This water ice plays a major role in the winter and spring evolution of the northern seasonal deposits. In particular the moving water ice annulus provides a strong source of atmospheric water vapor at low latitude and right from the end of northern winter. This localized and early vapor source above the water ice annulus is very probably underestimated or spatially diluted in most numerical general circulation models (GCMs). Very recent reanalysis of TES measurements of the spatial and temporal distribution of water vapor during three Martian years clearly shows "an annulus of water vapor growing above the edge of the retreating seasonal cap during spring" [Pankine et al., 2010]. Such a narrow and strong water vapor annulus (up to more than two times the column abundance of water vapor just a few degrees latitude away from the annulus) is clearly not simulated by GCMs. One important question is where is exactly located this water vapor in the atmosphere. These observations are column densities and there may be much more contrast between near-surface partial vapor pressures above and away from the 2° wide ice annulus water source because the water vapor will not mix rapidly vertically. Strong temperature gradients also occur between the receding CO_2-rich ice and the hotter dirty water ice annulus. This may favor strong near-surface poleward winds that will transport most of the vapor over the cold CO_2-rich ice and thus provide an efficient mechanism of supply for the cold-trapped water layer of fine water ice grains that we propose to overlie the CO_2-rich ice.

[60] What emerges from the OMEGA observations is a very dynamic behavior of water frost and water vapor, from subli-

mation of the water ice annulus and icy soil to recondensation of water vapor on top of the CO_2-rich ice. A water molecule is possibly subjected to a series of such events during the whole seasonal ices retreat, and this near surface process coupled with the katabatic wind events may strongly contribute to accumulation of water ice on the permanent polar cap and, possibly, preferentially at some specific places. Water frost budget may be thus variable over the polar cap.

[61] This evolution scenario has to be tested by modeling temporal sets of spectra for characteristic regions. Spectral modeling will provide more quantitative information on the deposits and their evolutions: organization of the ices and dust components, grain sizes, fraction of ground covered by ices, mixing ratio, dust content and thickness of the water ice layers. It will thus help to understand the various microphysical processes occurring during the deposition, condensation and sublimation stages of the seasonal ices. These processes should strongly constrain the spatial distribution and temporal evolution of fluxes of volatiles between the atmosphere and the surface, useful information for models of the Martian climate. Knowledge of the localization, volatility and mobility through the atmosphere of the various water sources may lead to improved Martian climatic models and improve our comprehension of the Martian water cycle.

References

Aharonson, O., M. T. Zuber, D. E. Smith, G. A. Neumann, W. C. Feldman, and T. H. Prettyman (2004), Depth, distribution, and density of CO_2 deposition on Mars, *J. Geophys. Res.*, *109*, E05004, doi:10.1029/2003JE002223.

Antoniadi, E. M. (1930), *La Planète Mars: Etude basée sur les résultats obtenus avec la grande lunette de l'observatoire de Meudon et exposé analytique de l'ensemble des travaux exécutés sur cet astre depuis 1659*, Hermann, Paris.

Bass, D. S., and D. A. Paige (2000), Variability of Mars' North Polar Water Ice Cap. II. Analysis of Viking IRTM and MAWD, *Icarus*, *144*, 397–409, doi:10.1006/icar.1999.6301.

Bass, D. S., K. E. Herkenhoff, and D. A. Paige (2000), Variability of Mars' North Polar Water Ice Cap. I. Analysis of Mariner 9 and Viking Orbiter Imaging Data, *Icarus*, *144*, 382–396, doi:10.1006/icar.1999.6300.

Beck, P., A. Pommerol, B. Schmitt, and O. Brissaud (2010), Kinetics of water adsorption on minerals and the breathing of the Martian regolith, *J. Geophys. Res.*, *115*, E10011, doi:10.1029/2009JE003539.

Benson, J. L., and P. B. James (2005), Yearly comparisons of the Martian polar caps: 1999–2003 Mars Orbiter Camera observations, *Icarus*, *174*, 513–523, doi:10.1016/j.icarus.2004.08.025.

Bibring, J.-P., et al. (2004), OMEGA: Observatoire pour la Minéralogie, l'Eau, les Glaces et l'Activité, in *Mars Express: the Scientific Payload*, edited by A. Wilson and A. Chicarro, *ESA Spec. Publ.*, ESA SP-1240, 37–49.

Bibring, J.-P., et al. (2005), Mars surface diversity as revealed by the OMEGA/Mars Express observations, *Science*, *307*, 1576–1581, doi:10.1126/science.1108806.

Briggs, C. B., and G. A. Leovy (1974), Mariner observations of the Mars north polar hood, *Bull. Am. Meteorol. Soc.*, *55*, 278–296, doi:10.1175/1520-0477(1974)055<0278:MOOTMN>42.0.CO;2.

Calvin, W. M., and T. Z. Martin (1994), Spatial variability in the seasonal south polar cap of Mars, *J. Geophys. Res.*, *99*, 21,143–21,152, doi:10.1029/94JE02011.

Cantor, B. A., M. J. Wolff, P. B. James, and E. Higgs (1998), Regression of Martian north polar cap: 1990–1997 Hubble Space Telescope observations, *Icarus*, *136*, 175–191, doi:10.1006/icar.1998.6020.

Cantor, B. A., P. B. James, M. Caplinger, and M. J. Wolff (2001), Martian dust storms: 1999 Mars Orbiter Camera observations, *J. Geophys. Res.*, *106*, 23,653–23,687, doi:10.1029/2000JE001310.

Cantor, B. A., P. B. James, and W. M. Calvin (2010), MARCI and MOC observations of the atmosphere and surface cap in the north polar region of Mars, *Icarus*, *208*, 61–81, doi:10.1016/j.icarus.2010.01.032.

Capen, C. F., and V. W. Capen (1970), Martian north polar cap, 1962–68, *Icarus*, *13*, 100–108, doi:10.1016/0019-1035(70)90121-1.

Caplinger, M. A., and M. C. Malin (2001), Mars Orbiter Camera geodesy campaign, *J. Geophys. Res.*, *106*, 23,595–23,606, doi:10.1029/2000JE001341.

Christensen, P. R., and R. W. Zurek (1984), Martian north polar hazes and surface ice: Results from the Viking Survey/Completion mission, *J. Geophys. Res.*, *89*, 4587–4596, doi:10.1029/JB089iB06p04587.

Christensen, P. R., et al. (2001), Mars Global Surveyor Thermal Emission Spectrometer experiment: Investigation description and surface science results, *J. Geophys. Res.*, *106*, 23,823–23,871, doi:10.1029/2000JE001370.

Clancy, R. T., B. J. Sandor, M. J. Wolff, P. R. Christensen, M. D. Smith, J. C. Pearl, B. J. Conrath, and R. J. Wilson (2000), An intercomparison of ground-based millimeter, MGS TES, and Viking atmospheric temperature measurements: Seasonal and interannual variability of temperatures and dust loading in the global Mars atmosphere, *J. Geophys. Res.*, *105*, 9553–9571, doi:10.1029/1999JE001089.

Cull, S., R. E. Arvidson, M. Mellon, S. Wiseman, R. Clark, T. Titus, R. V. Morris, and P. McGuire (2010), Seasonal H_2O and CO_2 ice cycles at the Mars Phoenix landing site: 1. Prelanding CRISM and HiRISE observations, *J. Geophys. Res.*, *115*, E00D16, doi:10.1029/2009JE003340.

Douté, S. (2009), Retrieving Mars surface reflectance from OMEGA/MEX imagery, in *WHISPERS '09: First Workshop on Hyperspectral Image and Signal Processing: Evolution in Remote Sensing, 2009*, pp. 1–4, IEEE, Piscataway N. J., doi:10.1109/WHISPERS.2009.5289063.

Douté, S., and B. Schmitt (1998), A multilayer bidirectional reflectance model for the analysis of planetary surface hyperspectral images at visible and near-infrared wavelengths, *J. Geophys. Res.*, *103*, 31,367–31,389, doi:10.1029/98JE01894.

Dumont, M., O. Brissaud, G. Picard, B. Schmitt, J.-C. Gallet, and Y. Arnaud (2010), High-accuracy measurements of snow bidirectional reflectance distribution function at visible and NIR wavelengths: Comparison with modeling results, *Atmos. Chem. Phys.*, *10*, 2507–2520, doi:10.5194/acp-10-2507-2010.

Eluszkiewicz, J. (1993), On the microphysical state of the Martian seasonal caps, *Icarus*, *103*, 43–48, doi:10.1006/icar.1993.1056.

Fischbacher, G. E., L. J. Martin, and W. A. Baum (1969), Seasonal behavior of the Martian polar caps, *Publ. Astron. Soc. Pac.*, *81*, 538.

Forget, F., F. Hourdin, and O. Talagrand (1998), CO_2 Snowfall on Mars: Simulation with a General Circulation Model, *Icarus*, *131*, 302–316, doi:10.1006/icar.1997.5874.

Forget, F., F. Hourdin, R. Fournier, C. Hourdin, O. Talagrand, M. Collins, S. R. Lewis, P. L. Read, and J.-P. Huot (1999), Improved general circulation models of the Martian atmosphere from the surface to above 80 km, *J. Geophys. Res.*, *104*, 24,155–24,175, doi:10.1029/1999JE001025.

Fray, N., and B. Schmitt (2009), Sublimation of molecules of astrophysical interest: A bibliographic review, *Planet. Space Sci.*, *57*, 2053–2080, doi:10.1016/j.pss.2009.09.011.

Grundy, W. M., and B. Schmitt (1998), The temperature-dependent near-infrared absorption spectrum of hexagonal H_2O ice, *J. Geophys. Res.*, *103*, 25,809–25,822, doi:10.1029/98JE00738.

Hansen, G. B. (2005), Ultraviolet to near-infrared absorption spectrum of carbon dioxide ice from 0.174 to 1.8 μm, *J. Geophys. Res.*, *110*, E11003, doi:10.1029/2005JE002531.

Hart, H. M., and B. M. Jakosky (1986), Composition and stability of the condensate observed at the Viking Lander 2 site on Mars, *Icarus*, *66*, 134–142, doi:10.1016/0019-1035(86)90013-8.

Herr, K. C., and G. C. Pimentel (1969), Infrared absorptions near three microns recorded over the polar cap of Mars, *Science*, *166*, 496–499, doi:10.1126/science.166.3904.496.

Hess, S. L., J. A. Ryan, J. E. Tillman, R. M. Henry, and C. B. Leovy (1980), The annual cycle of pressure on Mars measured by Viking landers 1 and 2, *Geophys. Res. Lett.*, *7*, 197–200, doi:10.1029/GL007i003p00197.

Hollingsworth, J. L., R. M. Haberle, A. F. C. Bridger, and J. Schaeffer (1995), Winter storm zones on Mars, in *Workshop on Mars Telescopic Observations, Proceedings of a Conference held 14–15 August, 1995 at Cornell University, Ithaca, NY*, edited by J. F. Bell III and J. E. Moersch, LPI Tech. Rep. 95-05, p. 15, Lunar and Planet. Inst., Houston, Tex.

Hollingsworth, J. L., R. M. Haberle, J. R. Barnes, A. F. C. Bridger, J. B. Pollack, H. Lee, and J. Schaeffer (1996), Orographic control of storm zones on Mars, *Nature*, *380*, 413–416, doi:10.1038/380413a0.

Houben, H., R. M. Haberle, R. E. Young, and A. P. Zent (1997), Modeling the Martian seasonal water cycle, *J. Geophys. Res.*, *102*, 9069–9083, doi:10.1029/97JE00046.

Hourdin, F., P. Le Van, F. Forget, and O. Talagrand (1993), Meteorological variability and the annual surface pressure cycle on Mars, *J. Atmos. Sci.*, *50*, 3625–3640, doi:10.1175/1520-0469(1993)050<3625:MVATAS>2.0.CO;2.

Iwasaki, K., Y. Saito, and T. Akabane (1979), Behavior of the Martian north polar cap, 1975–1978, *J. Geophys. Res.*, *84*, 8311–8316, doi:10.1029/JB084iB14p08311.

Iwasaki, K., Y. Saito, and T. Akabane (1982), Martian north polar cap 1979–1980, *J. Geophys. Res.*, *87*, 10,265–10,269, doi:10.1029/JB087iB12p10265.

Iwasaki, K., D. C. Parker, S. Larson, and T. Akabane (1999), Martian north polar cap 1996–1997, *Icarus*, *138*, 20–24, doi:10.1006/icar.1998.6061.

James, P. B. (1979), Recession of Martian north polar cap: 1977–1978 Viking observations, *J. Geophys. Res.*, *84*, 8332–8334, doi:10.1029/JB084iB14p08332.

James, P. B. (1982), Recession of Martian north polar cap: 1979–1980 Viking observations, *Icarus*, *52*, 565–569, doi:10.1016/0019-1035(82)90016-1.

James, P. B. (1985), Martian local dust storms, in *Recent Advances in Planetary Meteorology*, pp. 85–99, Cambridge Univ. Press, Cambridge, U. K.

James, P. B., and B. A. Cantor (2001), Martian north polar cap recession: 2000 Mars Orbiter Camera observations, *Icarus*, *154*, 131–144, doi:10.1006/icar.2001.6653.

James, P. B., R. T. Clancy, S. W. Lee, L. J. Martin, R. B. Singer, E. Smith, R. A. Kahn, and R. W. Zurek (1994), Monitoring Mars with the Hubble Space Telescope: 1990–1991 observations, *Icarus*, *109*, 79–101, doi:10.1006/icar.1994.1078.

Jones, K. L., R. E. Arvidson, E. A. Guinness, S. L. Bragg, S. D. Wall, C. E. Carlston, and D. G. Pidek (1979), One Mars year: Viking Lander imaging observations, *Science*, *204*, 799–806, doi:10.1126/science.204.4395.799.

Jouglet, D., F. Poulet, R. E. Milliken, J. F. Mustard, J.-P. Bibring, Y. Langevin, B. Gondet, and C. Gomez (2007), Hydration state of the Martian surface as seen by Mars Express OMEGA: 1. Analysis of the 3 μm hydration feature, *J. Geophys. Res.*, *112*, E08S06, doi:10.1029/2006JE002846.

Kieffer, H. H. (1979), Mars south polar spring and summer temperatures: A residual CO_2 frost, *J. Geophys. Res.*, *84*, 8263–8288, doi:10.1029/JB084iB14p08263.

Kieffer, H. H. (2007), Cold jets in the Martian polar caps, *J. Geophys. Res.*, *112*, E08005, doi:10.1029/2006JE002816.

Kieffer, H. H., and T. N. Titus (2001), TES mapping of Mars' north seasonal cap, *Icarus*, *154*, 162–180, doi:10.1006/icar.2001.6670.

Kieffer, H. H., T. N. Titus, K. F. Mullins, and P. R. Christensen (2000), Mars south polar spring and summer behavior observed by TES: Seasonal cap evolution controlled by frost grain size, *J. Geophys. Res.*, *105*, 9653–9699, doi:10.1029/1999JE001136.

Langevin, Y., F. Poulet, J.-P. Bibring, B. Schmitt, S. Douté, and B. Gondet (2005), Summer evolution of the north polar cap of Mars as observed by OMEGA/Mars Express, *Science*, *307*, 1581–1584, doi:10.1126/science.1109438.

Langevin, Y., S. Douté, M. Vincendon, F. Poulet, J. Bibring, B. Gondet, B. Schmitt, and F. Forget (2006), No signature of clear CO_2 ice from the 'cryptic' regions in Mars' south seasonal polar cap, *Nature*, *442*, 790–792, doi:10.1038/nature05012.

Langevin, Y., J.-P. Bibring, F. Montmessin, F. Forget, M. Vincendon, S. Douté, F. Poulet, and B. Gondet (2007), Observations of the south seasonal cap of Mars during recession in 2004–2006 by the OMEGA visible/near-infrared imaging spectrometer on board Mars Express, *J. Geophys. Res.*, *112*, E08S12, doi:10.1029/2006JE002841.

Larson, H. P., and U. Fink (1972), Identification of carbon dioxide frost on the Martian polar caps, *Astrophys. J.*, *171*, L91, doi:10.1086/180875.

Leovy, C. B., G. A. Briggs, A. T. Young, B. A. Smith, J. B. Pollack, E. N. Shipley, and R. L. Wildey (1972), The Martian atmosphere: Mariner 9 television experiment progress report (A 4.5), *Icarus*, *17*, 373, doi:10.1016/0019-1035(72)90006-1.

Lewis, S. R., M. Collins, P. L. Read, F. Forget, F. Hourdin, R. Fournier, C. Hourdin, O. Talagrand, and J. Huot (1999), A climate database for Mars, *J. Geophys. Res.*, *104*, 24,177–24,194, doi:10.1029/1999JE001024.

Li, W., K. Stamnes, H. Eide, and R. Spurr (2007), Bidirectional reflectance distribution function of snow: corrections for the Lambertian assumption in remote sensing applications, *Opt. Eng.*, *46*(6), 066201, doi:10.1117/1.2746334.

Malin, M. C., and K. S. Edgett (2001), Mars Global Surveyor Mars Orbiter Camera: Interplanetary cruise through primary mission, *J. Geophys. Res.*, *106*, 23,429–23,570, doi:10.1029/2000JE001455.

Milliken, R. E., J. F. Mustard, F. Poulet, D. Jouglet, J.-P. Bibring, B. Gondet, and Y. Langevin (2007), Hydration state of the Martian surface as seen by Mars Express OMEGA: 2. H_2O content of the surface, *J. Geophys. Res.*, *112*, E08S07, doi:10.1029/2006JE002853.

Mitrofanov, I. G., et al. (2003), CO_2 Snow Depth and Subsurface Water-Ice Abundance in the Northern Hemisphere of Mars, *Science*, *300*, 2081–2084, doi:10.1126/science.1084350.

Neugebauer, G., G. Miinch, H. Kieffer, S. C. Chase Jr., and E. Miner (1971), Mariner 1969 infrared radiometer results: Temperatures and thermal properties of the Martian surface, *Astron. J.*, *76*, 719–727, doi:10.1086/111189.

Ockert-Bell, M. E., J. F. Bell, J. B. Pollack, C. P. McKay, and F. Forget (1997), Absorption and scattering properties of the Martian dust in the solar wavelengths, *J. Geophys. Res.*, *102*, 9039–9050, doi:10.1029/96JE03991.

Owen, T. (1982), The composition of the Martian atmosphere, *Adv. Space Res.*, *2*, 75–80, doi:10.1016/0273-1177(82)90107-7.

Paige, D. A., Jr. (1985), The annual heat balance of the Martian polar caps from Viking observations, Ph.D. thesis, Calif. Inst. of Technol., Pasadena.

Pankine, A. A., L. K. Tamppari, and M. D. Smith (2010), MGS TES observations of the water vapor above the seasonal and perennial ice caps during northern spring and summer, *Icarus*, *210*, 58–71, doi:10.1016/j.icarus.2010.06.043.

Pommerol, A., and B. Schmitt (2008a), Strength of the H_2O near-infrared absorption bands in hydrated minerals: Effects of particle size and correlation with albedo, *J. Geophys. Res.*, *113*, E10009, doi:10.1029/2007JE003069.

Pommerol, A., and B. Schmitt (2008b), Strength of the H_2O near-infrared absorption bands in hydrated minerals: Effects of measurement geometry, *J. Geophys. Res.*, *113*, E12008, doi:10.1029/2008JE003197.

Pommerol, A., B. Schmitt, P. Beck, and O. Brissaud (2009), Water sorption on martian regolith analogs: Thermodynamics and near-infrared reflectance spectroscopy, *Icarus*, *204*, 114–136, doi:10.1016/j.icarus.2009.06.013.

Portyankina, G., W. J. Markiewicz, N. Thomas, C. J. Hansen, and M. Milazzo (2010), HiRISE observations of gas sublimation-driven activity in Mars' southern polar regions: III. Models of processes involving translucent ice, *Icarus*, *205*, 311–320, doi:10.1016/j.icarus.2009.08.029.

Quirico, E., and B. Schmitt (1997), Near-Infrared Spectroscopy of Simple Hydrocarbons and Carbon Oxides Diluted in Solid N_2 and as Pure Ices: Implications for Triton and Pluto, *Icarus*, *127*, 354–378, doi:10.1006/icar.1996.5663.

Schmidt, F., S. Douté, B. Schmitt, M. Vincendon, J. Bibring, Y. Langevin, and OMEGA Team (2009), Albedo control of seasonal south polar cap recession on Mars, *Icarus*, *200*, 374–394, doi:10.1016/j.icarus.2008.12.014.

Schmitt, B., E. Quirico, F. Trotta, and W. Grundy (1998), Optical properties of ices from UV to infrared, in *Solar System Ices, Astrophys. Space Sci. Lib.*, vol. 227, edited by B. Schmitt, C. de Bergh, and M. Festou, pp. 199–240, Kluwer Acad., Dordrecht, Netherlands.

Schmitt, B. S. Douté, Y. Langevin, F. Poulet, J.-P. Bibring, B. Gondet, and The Omega Team (2005), Northern seasonal condensates on Mars by OMEGA/Mars Express, paper presented at 36th Annual Lunar and Planetary Science Conference, Lunar and Planet. Inst., Houston, Tex.

Smith, D. E., M. T. Zuber, and G. A. Neumann (2001), Seasonal variations of snow depth on Mars, *Science*, *294*, 2141–2146, doi:10.1126/science.1066556.

Smith, M. D. (2004), Interannual variability in TES atmospheric observations of Mars during 1999–2003, *Icarus*, *167*, 148–165, doi:10.1016/j.icarus.2003.09.010.

Soderblom, L. A., M. C. Malin, J. A. Cutts, and B. C. Murry (1973), Mariner 9 observations of the surface of Mars in the north polar region, *J. Geophys. Res.*, *78*, 4197–4210, doi:10.1029/JB078i020p04197.

Svitek, T., and B. Murray (1990), Winter frost at Viking Lander 2 site, *J. Geophys. Res.*, *95*, 1495–1510, doi:10.1029/JB095iB02p01495.

Tamppari, L. K., M. D. Smith, D. S. Bass, and A. S. Hale (2008), Water-ice clouds and dust in the north polar region of Mars using MGS TES data, *Planet. Space Sci.*, *56*, 227–245, doi:10.1016/j.pss.2007.08.011.

Tillman, J. E., N. C. Johnson, P. Guttorp, and D. B. Percival (1993), The Martian annual atmospheric pressure cycle: Years without great dust storms, *J. Geophys. Res.*, *98*, 10,963–10,971, doi:10.1029/93JE01084.

Titus, T. N. (2009), Mars polar cap edges tracked over four full Mars years using MGS TES, *LPI Contrib.*, *1494*, 57–58.

Titus, T. N., H. H. Kieffer, K. F. Mullins, and P. R. Christensen (2001), TES premapping data: Slab ice and snow flurries in the Martian north polar night, *J. Geophys. Res.*, *106*, 23,181–23,196, doi:10.1029/2000JE001284.

Vincendon, M., Y. Langevin, F. Poulet, J.-P. Bibring, and B. Gondet (2007), Recovery of surface reflectance spectra and evaluation of the optical depth of aerosols in the near-IR using a Monte Carlo approach: Application to the OMEGA observations of high-latitude regions of Mars, *J. Geophys. Res.*, *112*, E08S13, doi:10.1029/2006JE002845.

Wagstaff, K. L., T. N. Titus, A. B. Ivanov, R. Castaño, and J. L. Bandfield (2008), Observations of the north polar water ice annulus on Mars using THEMIS and TES, *Planet. Space Sci.*, *56*, 256–265, doi:10.1016/j.pss.2007.08.008.

Wang, H., and A. P. Ingersoll (2002), Martian clouds observed by Mars Global Surveyor Mars Orbiter Camera, *J. Geophys. Res.*, *107*(E10), 5078, doi:10.1029/2001JE001815.

Warren, S. G. (1982), Optical properties of snow, *Rev. Geophys. Space Phys.*, *20*, 67–89, doi:10.1029/RG020i001p00067.

Zuber, M. T., et al. (1998), Observations of the north polar region of Mars from the Mars Orbiter Laser Altimeter, *Science*, *282*, 2053–2060, doi:10.1126/science.282.5396.2053.

T. Appéré, S. Douté, and B. Schmitt, Institut de Planétologie et d'Astrophysique de Grenoble, Université J. Fourier, CNRS/INSU, BP 53, F-38041 Grenoble CEDEX 9, France. (thomas.appere@obs.ujf-grenoble.fr)

J.-P. Bibring, B. Gondet, and Y. Langevin, Institut d'Astrophysique Spatiale, Université Paris-Sud XI, CNRS/INSU, Bat. 120-121, F-91405 Orsay CEDEX, France.

F. Forget and A. Spiga, Laboratoire de Météorologie Dynamique, IPSL, CNRS/INSU, Université Pierre et Marie Curie, BP 99, 4, place Jussieu, F-75005 Paris CEDEX 05, France.

A. Pommerol, Physikalisches Institut, Universität Bern, Sidlerstrasse 5, CH-3012 Bern, Switzerland.